J. Fluid Mech. (1998), *vol.* 363, *pp.* 115–151. Printed in the United Kingdom

Secondary flow induced by riblets

By D. B. GOLDSTEIN AND T.-C. TUAN

Department of Aerospace Engineering and Engineering Mechanics,
The University of Texas at Austin, Austin, TX 78712, USA

(Received 17 September 1996 and in revised form 30 August 1997)

The effects of riblets on one wall of a channel bounding fully developed turbulent flow are investigated. Various perturbation elements including wires, fins and slots are modelled in order to understand the effects of riblets. It is found that widely spaced riblets, fins and wires create a substantial increase in turbulent activity just above the element. These elements are also found to produce a remarkable pattern of secondary mean flows consisting of matched pairs of streamwise vortices. The secondary flows occur only if the bulk flow is turbulent and their characteristics depend on element geometry. It is suggested that these secondary flows are strongly linked with the increase in drag experienced by widely spaced riblets in experimental studies. The secondary flows are probably caused by two-dimensional spanwise sloshing of the flow, inherent in a turbulent boundary layer, interacting with the stream-aligned element. This two-dimensional mechanism is investigated with a series of two-dimensional simulations of sloshing flow over isolated elements. Grid resolution and domain size checks are made throughout the investigation.

1. Introduction

It has been found experimentally that surfaces possessing ridges (riblets) are capable of reducing turbulent flow skin friction. Effective riblets generally consist of streamwise ridges having triangular, cusped, or rectangular cross-sections and, in fact, plastic film having sub-millimetre-scale triangular riblets has been developed commercially for surface application. Walsh (1990) and Coustols & Savill (1992) provide comprehensive reviews of the experimental and early computational studies on the riblet drag reduction effect. Walsh suggests, as have others (see Bacher & Smith 1985; Bechert *et al.* 1986, 1989, 1997*b*; Bechert & Bartenwerfer 1989; Coustols & Savill 1992 and Luchini *et al.* 1991), that riblets work by effectively providing an enhanced cross-stream resistance to the near-wall motion above the riblet crests.

While riblets decrease drag in some cases they increase it in others and, overall, experimental drag reduction obtained from riblet surfaces has been disappointing – generally less than 10%. While riblets roughly 10 wall units high and spaced by 10–30 wall units usually produce a drag reduction, if they are taller or more widely spaced they most often produce a drag increase or at least no drag benefit.

Recent computational work using direct numerical simulation (DNS) provides detailed flow statistics unavailable experimentally. The conclusions drawn from the simulations have been generally similar to those reached based on experiments alone due to the complicated physics involved; there are many effects associated with (and perhaps multiple causes of) the drag reduction.

Choi, Moin & Kim (1991) used a finite difference approach to simulate steady laminar flow over riblets. They found that the drag increase characteristic of laminar flow became more pronounced as the ribs projected further into their channel. They also argued that there should be no secondary flow (wall normal or spanwise motion) associated with such laminar flow. Choi, Moin & Kim (1993) have also extended their calculations to turbulent flow and found general agreement with experiments. While they report only minor differences between the 45° and 60° geometries, there were interesting findings from increasing the crest-to-crest spacing. Of particular interest, they found that over 60° riblets spaced at 20 wall units the turbulence intensity and Reynolds shear stresses are reduced while over larger drag-increasing riblets spaced at 40 wall units, these quantities are increased. They attribute the drag increase to the ability of the streamwise vortices to lie in the larger riblet valleys thus exposing a larger surface area to the vortex-induced sweep motion. They also find a secondary flow consisting of a vortex pair which produces upflow over rib crests and downflow in the valleys and they note the similarity to secondary flows in ducts of non-circular cross-section. The larger riblets had much stronger secondary flows than did the smaller drag-reducing riblets. Choi *et al.* conclude that it is unclear how the secondary flow affects drag performance.

Chu, Henderson & Karniadakis (1992) and Chu & Karniadakis (1993) provide detailed turbulence statistics and find that all three components of turbulence intensity and the Reynolds shear stress are reduced above both riblet crests and valleys in the drag-reducing regime. They found a qualitative increase in streak spacing due to riblets. They also describe transient secondary flows in riblet valleys due to the presence of large streamwise boundary layer vortices and suggest that the 'lateral resistance offered by the riblets produces secondary flow and vortical structures in the riblet valleys'. They do not, however, explicitly describe mean secondary flows.

Crawford (1994) used quadrant analysis and confirmed that the effect of drag-reducing riblets is confined to the buffer region immediately above the riblet crests. She finds that the intensity of the burst and sweep events is diminished over a ribbed surface and concludes that a mean flow up away from a riblet crest would reduce the riblet drag. Crawford & Karniadakis (1996) provide a Reynolds stress analysis of three riblet configurations and find secondary flows like those of Choi *et al.* (1993).

Goldstein, Handler & Sirovich (1995) used DNS to confirm that cross-flow damping near riblet crests causes the upward displacement of the streamwise streaks and vortices which in turn produces a drag-reduction. They also found that drag reducing riblets tend to pin the spanwise flow separation and re-attachment points on riblet crests. The idea would then arise that riblets with a spacing corresponding to the mean streamwise vortex spacing might pin the cross-flow separation/re-attachment sites and stabilize the vortices. Stable vortices might not tend to lift off the surface and cause the burst–sweep events responsible for much of the viscous drag. In fact, if the riblets were spaced slightly wider than the vortices, one might think that the pinning of stagnation stream surfaces would increase the mean vortex spacing and hence reduce the drag. Yet, these suppositions are misleading; widely spaced riblets do not reduce drag.

There have also been some recently published interesting experimental results. Park & Wallace (1993) used large riblets in a low-speed wind tunnel and made hot-wire measurements all the way into the riblet valleys. They found that for a drag-reducing riblet configuration the valley flow is slow and almost laminar and that turbulence intensities can be increased over the crests while decreased over the valleys. Suzuki & Kasagi (1994) used particle tracking velocimetry over riblets in both a drag-reducing ($S^+ = 15$) and a drag-neutral ($S^+ = 31$) configuration where S^+ is riblet

spacing, defined below. Whereas the $S^+ = 15$ riblets reduced all three r.m.s. velocity fluctuations, the $S^+ = 31$ case only reduced the streamwise component but increased the other two. Of particular note, Suzuki & Kasagi find that the widely spaced riblets induce a modest mean secondary flow while the more closely spaced riblets produced only an extremely weak secondary flow. These secondary flows appear consistent with the three Reynolds stresses they obtain and the trends they find agree with those found by the computations mentioned above.

While Goldstein *et al.* (1995) showed that progressively more widely spaced regions of cross-flow damping produce a diminishing drag benefit, it remains unclear why widely spaced real riblets should produce a drag increase. Perhaps an additional physical mechanism comes into play as the riblets become isolated. For example, small riblets having heights $H^+ \approx 10$ ($H^+ = hu^*/\nu$ for height h, friction velocity u^*, and kinematic viscosity ν) and spacings S^+ of 100 or more ($S^+ = su^*/\nu$ for spacing s) are nearly representative of single isolated ribs rather than an array of interacting elements. Riblets spaced more widely than a few streak spacings should not perceive the presence of their neighbours while closely spaced ribs should interact. That is, there ought be a transitional spacing, perhaps demarcated by the change in the skin friction drag (from beneficial to detrimental), where the physics of the flow changes from that of closely interacting elements to that of independent elements.

The above work concentrated on determining why some riblets work. One of the objectives of the present paper is to answer the (perhaps) easier question of why riblets stop working when they are spaced too widely. One might then approach the design of better surface textures from a different perspective. None of the work mentioned above provides a complete physical explanation of what changes in a flow as the riblet spacing is increased from a regime of closely interacting elements to that of isolated elements. The present paper is an exploration of the effects of riblet spacing and geometry on the physics of a turbulent boundary layer flow. We first briefly describe the computational method (§2). Section 3 presents the results of three separate simulations of flow over riblets spaced by $S^+ = 23$, 62.8, and 375. To elucidate the physical mechanisms which cause the various phenomena observed over riblets, particularly the causes of mean secondary flows, in §4 we examine flow over other longitudinal isolated near-surface elements, namely slots, wires and fins. We argue that the secondary flows are primarily due neither to a vorticity tilting mechanism nor to simply some form of Prandtl's secondary flow of the second kind. These interesting secondary flows are the most important feature of the present work and they are discussed in terms of spanwise two-dimensional sloshing flow over surface elements in §5.

2. The computational method

The present work uses an unconventional computational approach – solid surfaces are modelled by applying a body force to the flow so as to bring the flow to rest on a virtual surface. This approach for creating a virtual solid surface has been shown (Goldstein, Handler & Sirovich 1993*b*) to be sufficiently flexible and efficient to model laminar and turbulent flow over complicated geometries. That work also provides a discussion of the numerical stability of the method. Goldstein *et al.* (1995) provides a more detailed review of the virtual surface approach as well as grid resolution studies of laminar flow over riblets, an examination of the sensitivity of the solution to various smoothing parameters, and an in-depth analysis of turbulent flow over a virtual flat plate, and arrays of riblets, wires, and damping elements. Hence, only a brief summary of the virtual surface approach will now be given.

The basis of the virtual surface model is that the solid being modelled is defined by a set of boundary points which exist within a region also containing a fixed (Eulerian) mesh on which the flow equations are solved. The boundary points exert a body force on the fluid such that the flow comes to rest on the boundary. The fluid mediates the inter-point forces. A key accomplishment of the present approach is that flows around complex boundary geometries are reduced to ones which are fully rectilinear and hence are amenable to spectral methods. The virtual surface approach imposes only a small computational overhead (roughly 5% of the computational time in the calculations presented here) and little in the way of a coding burden. On the other hand, the introduction of a localized force field into a spectral approach detracts from the accuracy of the approach and grid convergence studies become more important.

For present purposes the incompressible Navier–Stokes equations with an external force field are written as follows:

$$\frac{\partial \boldsymbol{U}}{\partial t} = \boldsymbol{U} \times \Omega - \nabla(p/\rho + \tfrac{1}{2}(\boldsymbol{U} \cdot \boldsymbol{U})) + \nu \nabla^2 \boldsymbol{U} + \boldsymbol{f}, \tag{2.1a}$$

and

$$\nabla \cdot \boldsymbol{U} = 0. \tag{2.1b}$$

Here, t is time, $\boldsymbol{U} = (U, V, W)$ is the velocity in rectangular coordinates (x, y, z), Ω is the vorticity, p is the pressure, ρ is the density, and ν is the kinematic viscosity. The force $\boldsymbol{f}$, which is used to generate a virtual surface, is given by

$$\boldsymbol{f}(\boldsymbol{x}, t; \boldsymbol{x}_s) = \boldsymbol{g}(\boldsymbol{x}, t)\delta(\boldsymbol{x} - \boldsymbol{x}_s), \tag{2.2}$$

where the position vector $\boldsymbol{x}_s$ locates the bounding surface, $\boldsymbol{g}(\boldsymbol{x}, t)$ is a feedback forcing given in Goldstein *et al.* (1995), and δ is the three-dimensional delta function. Potential difficulties associated with the singular nature of the force field were addressed in Goldstein *et al.* (1993*b*, 1995). It is not necessary to bring the flow to rest within a solid. In fact, fluid will in general flow below the modelled riblet surface (inside the solid) while the velocity is forced to be zero on the riblet surface itself.

A spectral method (Kim, Moin & Moser 1987; Handler, Hendricks & Leighton 1989) is used to solve equations (2.1*a, b*). We consider a channel, periodic in the streamwise (x) and spanwise directions (z) and bounded by impermeable flat walls in the vertical direction (y). Flow quantities are represented by Fourier expansions in the horizontal (x, z)-plane and a Chebyshev expansion in the wall normal direction.

3. Turbulent flow over riblets

Riblets having a triangular or cusped U cross-section, a peak to peak spacing, S^+, of 10 to 20, and a height, H^+, of of 5 to 15 are found experimentally to be most effective in reducing drag (Walsh 1990). We first examine the turbulent flow over cusped riblets having $H^+ = 8.9$ and three different values of S^+. The channel modelled here has the orientation seen in figure 1. In the bulk of the domain between the ribbed surface and the top boundary a constant pressure gradient, G, is applied in the x-direction. The equations of motion (2.1*a, b*) are scaled in such a way that the non-dimensional pressure gradient in a channel without riblets is given by $G = (R^*/R_{cl})^2$, where $R^* = u^* y_{l/2}/\nu$ is the friction Reynolds number, $R_{cl} = u_{cl} y_{l/2}/\nu$ is the centreline Reynolds number, $y_{l/2}$ is the channel half-height, u_{cl} is the centreline velocity, u^* is given by $u^* = (\tau_w/\rho)^{1/2}$, and τ_w is the shear stress at the wall. The value of G is chosen so that the steady-state value of R^* is known *a priori* (≈ 125) and R_{cl} is about 2200.

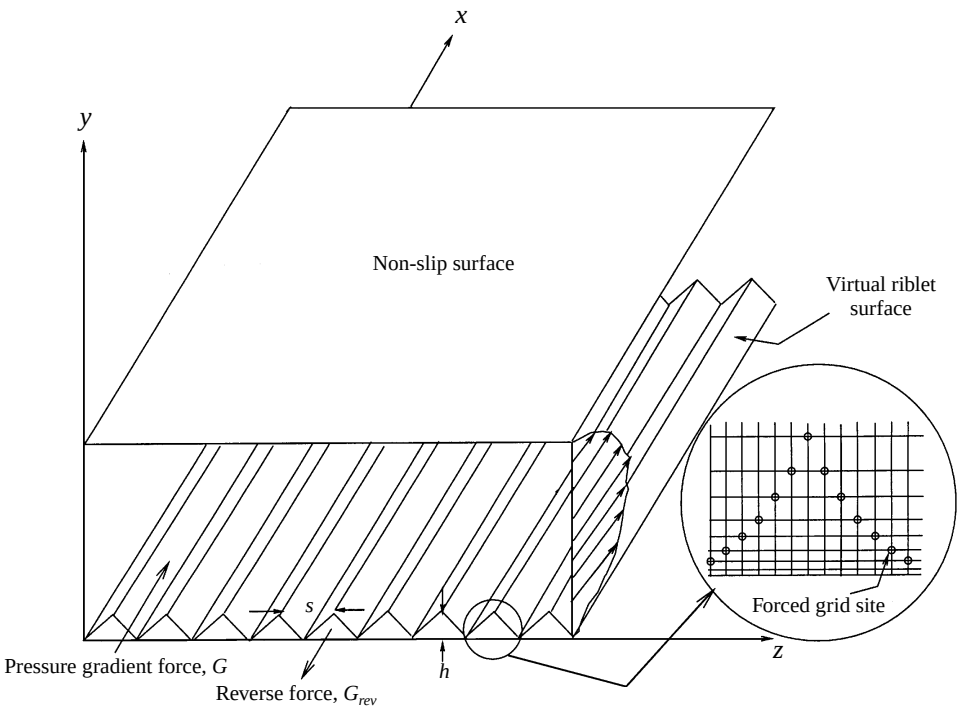

FIGURE 1. Geometry for the simulation of channel flow between two impermeable boundaries and containing a virtual riblet surface. A uniform pressure gradient is applied above the riblet and a pressure gradient of opposite sign is applied below. Forces are applied to riblet surface points to create a no-slip surface.

Accurate simulation of flow over riblets requires that each rib cross-section be represented by at least several grid points. As will be seen below, large-scale secondary flows may occur and the flow field domain must be large enough to capture them. The riblets may also stabilize the streamwise streaks and thereby increase the streamwise extent of velocity correlations beyond that found in flat-plate boundary layers. Hence, the minimum channel of Jimenez & Moin (1991) for modelling sustained turbulence (roughly 250–350 wall units streamwise and 100 spanwise) is probably substantially too small. The present riblet simulations utilize nominal dimensions of 1875:250:375 viscous units in x:y:z as safe minimum estimates; these lengths are felt to be sufficient to capture the dominant flow physics. When secondary flows with a large spanwise extent are investigated, the domain width is varied to ensure domain size independence. Because of the severe resolution and temporal requirements implied by this discussion, it has been feasible to perform only a few detailed grid resolution studies of turbulent flow.

One of the quantities of interest will be the drag ratio, DR, between the ribbed wall and the opposing flat wall. The drag on the ribbed surface can be computed at any time from an instantaneous momentum balance involving the rate of change of momentum, the drag on the flat surface (both of which can be computed precisely at any instant), and the pressure gradient force.

In this section are presented flow results for three different riblet spacings of $S^+ =$ 23, 62.8, and 375. For the first and last configurations, progressive grid-doubling convergence studies were run for fully turbulent flow. The $S^+ = 23$ riblets produce

the expected drag decrease while the other two configurations produce a small drag increase. All the riblets are small and of the same shape; only the amount of flat surface between the ribs is varied.

3.1. *Drag-reducing configuration*

Riblets are created by applying the force field along a sequence of grid sites near the lower channel boundary (figure 1) which form a cusped shape due to the cosine grid. For the $S^+ = 23$ configuration at the lowest resolution (case 1) the peak-to-peak spacing of the ribs is 8 grid sites (12 sites on the 3/2's de-aliasing grid), the ribs are seven grid sites high, and there are 16 riblets along the channel width.

There is a small space between the shear-free lower flow field boundary and the riblet no-slip surface. In this space a force in the $-x$-direction, G_{rev}, as described in Goldstein *et al.* (1993*b*, 1995), is applied to create a flow inside the ribs that reduces the kinks that otherwise develop in the mean velocity profile. The value of G_{rev} is small ($-16G$) below the rib peaks and large ($-120G$) below the valleys. These values as well as other run parameters for all turbulent runs are given in table 1.

The simulation begins with the abrupt insertion of the ribbed virtual surface into an equilibrium turbulent channel flow followed by the relaxation of the flow over several large eddy turn-over times, $T_e = 2y_{l/2}/(u')_{max}$, where $(u')_{max}$ is the maximum root-mean-square streamwise turbulence intensity. (The flow was usually allowed to relax for more than 10 000 time steps or about $7.7T_e$.) The autocorrelation of the drag ratio was used to confirm the number of time steps between independent flow field realizations (24 realizations in this simulation). The total integration time was $T^+ = 7567$ where $T^+ = (N_{step}\Delta t)u^{*2}/\nu$, and $N_{step}\Delta t$ is the computational time. The time step used is $\Delta t u^{*2}/\nu = 0.076$.

Typical instantaneous results are shown in figure 2. Contours of constant streamwise velocity and enstrophy are shown along with velocity vectors in the (y, z) and (x, z)-planes. There is ordinary turbulent channel flow in the bulk of the domain indicated by streamwise vortices which draw slow-moving fluid away from the walls (creating low-speed streaks, figure 2*c*) and bring high-speed fluid toward the walls. Such vortices are known to persist near a wall (Robinson 1991; Brooke & Hanratty 1993; Bernard, Thomas & Hander 1993). It is evident in this snapshot that there are few easily apparent qualitative differences between the structures above the riblets and near the flat wall. This is as expected based on the work cited in §1.

To display detailed mean flow statistics we first average in the x-direction and time. We then average over all of the 16 riblets and once more across the riblet centreline. Figure 3 provides contours of several properties over an average riblet along with velocity vectors in the (y, z)-plane (figure 3*a*). Also shown for comparison are the contours of the same quantities found over the opposite flat wall. $\bar{U}$ denotes the local mean velocity, u', v', and w' indicate root-mean-square fluctuating velocities while u, v, and w indicate fluctuating velocities. In addition, length scales made non-dimensional by the viscous scale l^* ($l^* \equiv \nu/u^*$) will be denoted by a $+$ superscript, e.g. $y^+ \equiv y/l^*$ where the height y is measured with respect to the flat wall or the riblet valley, as appropriate. The viscous scales used in the contour plots (u^* and l^*) are nominal values for a similar channel having two flat walls.

In figure 3(*a*) one sees that the mean streamwise velocity contours arch up over the riblet and are closely spaced over the crest while being widely spaced over the valley. This corresponds to high shear stress on the rib crest and low stress in the

† Animations are available on the Web at www.ae.utexas.edu/~tuan/research.html.

Case no.	1	2	3	4	5	6	7	8	9	10	11	12	13	14	15
Case desig.	rclo	rchi	rchst	rfar	risollo	risolhi	s27b3	s29b3lo	s29b3hi	w9b3	w11b3	w9b5	w11b5	f11b5	df11b5
N_x	64	64	48	64	64	64	64	64	64	64	64	64	64	64	64
N_y	65	129	257	65	65	129	65	65	129	65	65	65	65	65	65
N_z	128	256	512	128	128	256	128	128	256	128	128	128	128	128	128
L_x	15	15	11.25	15	15	15	15	15	15	15	15	15	15	15	15
L_z	3	3	3	3	3	3	3	3	3	3	5	5	5	5	5
$l^* \times 10^{3\dagger}$	8.1285	8.1629	8.1057	7.9575	7.9908	7.9799	8.0425	8.1654	8.1546	7.9126	7.645	7.9121	7.7760	8.1117	8.1074
$u^* \times 10^{2\dagger}$	3.076	3.063	3.084	3.142	3.129	3.133	3.11	3.062	3.066	3.16	3.27	3.16	3.12	3.09	3.07
$\Delta t^+ \times 10^2$	7.567	3.752	1.903	7.896	7.830	3.926	6.96	6.749	3.760	7.19	7.70	7.19	7.01	6.87	6.79
T^+	7567	7503	1903	7896	15660	7067	4176	16198	6767	10785	8470	7100	7010	3435	4074
ϵ	2	2	2	2	2	2	2	2	2	2	2	2	2	2	2
(ξ_1, ξ_2)	$(20,-3)$	$(20,-3)$	$(20,-3)$	$(20,-3)$	$(20,-3)$	$(20,-3)$	$(20,-3)$	$(20,-3)$	$(20,-3)$	$(20,-3)$	$(20,-3)$	$(20,-3)$	$(20,-3)$	$(20,-3)$	$(20,-3)$
$(\alpha\Delta t, \beta)$	(20,20)	(20,30)	(200,20)	(20,20)	(20,20)	(20,30)	(20,20)	(20,20)	(80,20)	(20,20)	(20,20)	(20,20)	(20,20)	(20,20)	(20,20)
G_{rev}	16–120	10–70	16–120	16–120	16–120	10–70	4–800	4–800	16–120	NA	NA	NA	NA	NA	NA
S^+	23.07	22.97	23.13	62.8	375.4	375.9	373.0	367.4	367.9	379.1	392.4	632.0	643.0	616.4	616.7
H^+	8.77	8.74	8.80	8.96	8.92	8.94	5.20	9.17	9.19	9.17	15.3	9.46	15.0	14.4	14.4
DR	0.968	0.954	0.960	1.038	1.012	1.015	1.004	0.991	0.990	1.045	1.194	1.044	1.129	1.012	0.988
DR error bar	$\pm$0.015	$\pm$0.016	$\pm$0.017	$\pm$0.018	$\pm$0.010	$\pm$0.020	$\pm$0.020	$\pm$0.013	$\pm$0.022	$\pm$0.015	$\pm$0.034	$\pm$0.014	$\pm$0.016	$\pm$0.016	$\pm$0.022
Tot. steps$\times 10^{-3}$	100	200	100	100	200	180	60	240	180	150	110	100	100	50	60
Steps/indep. real.	3700	8600	6800	2800	2800	7050	3000	3850	9350	3600	8750	3300	3350	2600	4800
Λ^+	98.0	97.6	98.3	94.3	105.6	96.9	93.2	103.3	100.6	106.6	112	98.6	105	106	115.6
$y^+_{R_{uu_{min}}}$	19.8	19.7	18.5	17.0	14.0	12.6	12.3	13.8	13.0	13.9	18.5	12.0	12.2	17.4	15.9
Secondary flow	yes?	yes	yes	yes	yes	yes	no	yes	yes	yes	yes	yes	yes	yes	yes
Core spacing	NA	10.8	10.9	29.7	58.6	55.5	NA	59.8	66.3	54	30	37	27	59	69
Core height	NA	12.9	12.5	24.6	35.8	33.5	NA	32.3	34.1	35	20.5	25	18	44	47
$\overline{V}_{max}/u^*$	?	0.030	0.039	0.122	0.320	0.350	NA	-0.070	-0.105	0.272	?	0.174	?	0.359	0.527
Tertiary flow	no	no	no	no	yes	yes	no	yes	yes	yes	yes	yes	yes	?	yes
Core spacing	NA	NA	NA	NA	208.8	190.3	NA	181.5	219.6	210	198	151	201	?	240
Core height	NA	NA	NA	NA	34.4	33.2	NA	30.4	42.4	33	50	33	53	?	29
Vertical extent	NA	NA	NA	NA	NA	106.5	NA	NA	NA	60	125	60	125	?	?

† In this table l^* and u^* are span-averaged values for the riblet side of channel.

TABLE 1. Turbulent simulations: Case, Reference case number; N_x, Number of modes in x (streamwise) direction; N_y, Number of modes in y (wall normal) direction; N_z, Number of modes in z (cross flow) direction; L_x, Domain length in x-direction; L_z, Domain width in z-direction; Δt^+, Normalized time step, $\Delta t u^{*2}/\nu$; T^+, Total normalized run time, $T u^{*2}/\nu$; ϵ, Measure of Gaussian width (see eqn. 6 in Goldstein *et al.* 1995); (ξ_1, ξ_2), Decay constants (see eqn. 7 in Goldstein *et al.* 1995); $(\alpha\Delta t, \beta)$, Force field gains (see eqn. 3 in Goldstein *et al.* 1995); G_{rev}, Magnitude of reverse pressure gradient below rib / pressure gradient above; S^+, Normalized element-to-element spacing; H^+, Normalized element height; DR, Drag ratio of riblet side to flat side; Tot. steps, Total number of time steps in simulation; Λ^+, Normalized low-speed streak spacing; $y^+_{R_{uu_{min}}}$, Normalized height of the minimum in R_{uu} over the flat surface; Core spacing, Normalized core to core spacing for secondary and tertiary vorticies; Core height, Normalized core height for secondary and tertiary vortices; Vertical extent, Normalized height of secondary flow stagnation point; NA, Not applicable for the run; ?, Inconclusive for the run.

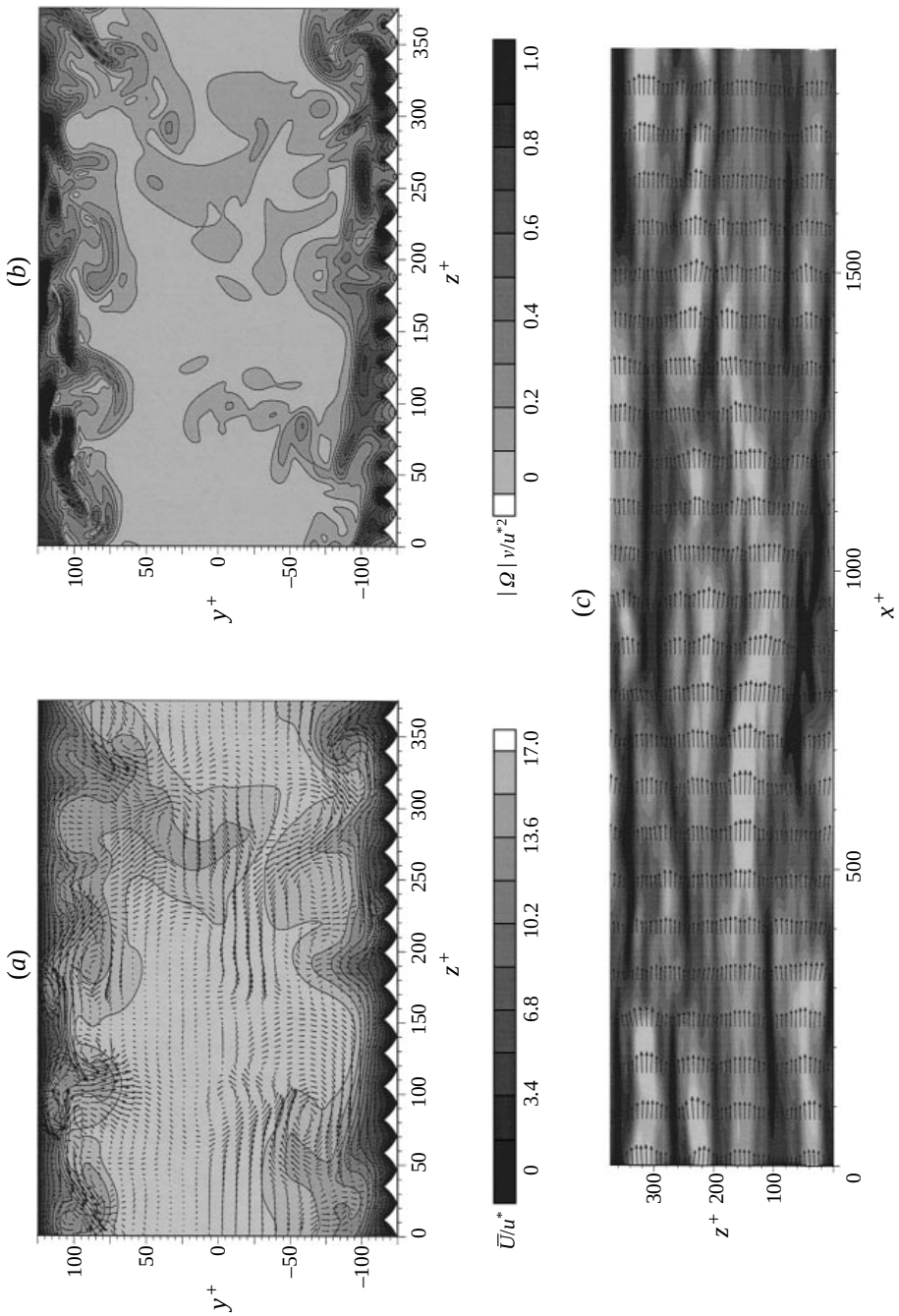

FIGURE 2. Instantaneous contours over an $S^+ = 23$, $H^+ = 8.7$ riblet array (case 2). (*a*) Streamwise velocity contours and vectors in a (y, z)-plane at $x^+ = 0$. (*b*) Enstrophy contours in the same (y, z)-plane. (*c*) Streamwise velocity contours and vectors $11l^*$ above the riblet valleys.

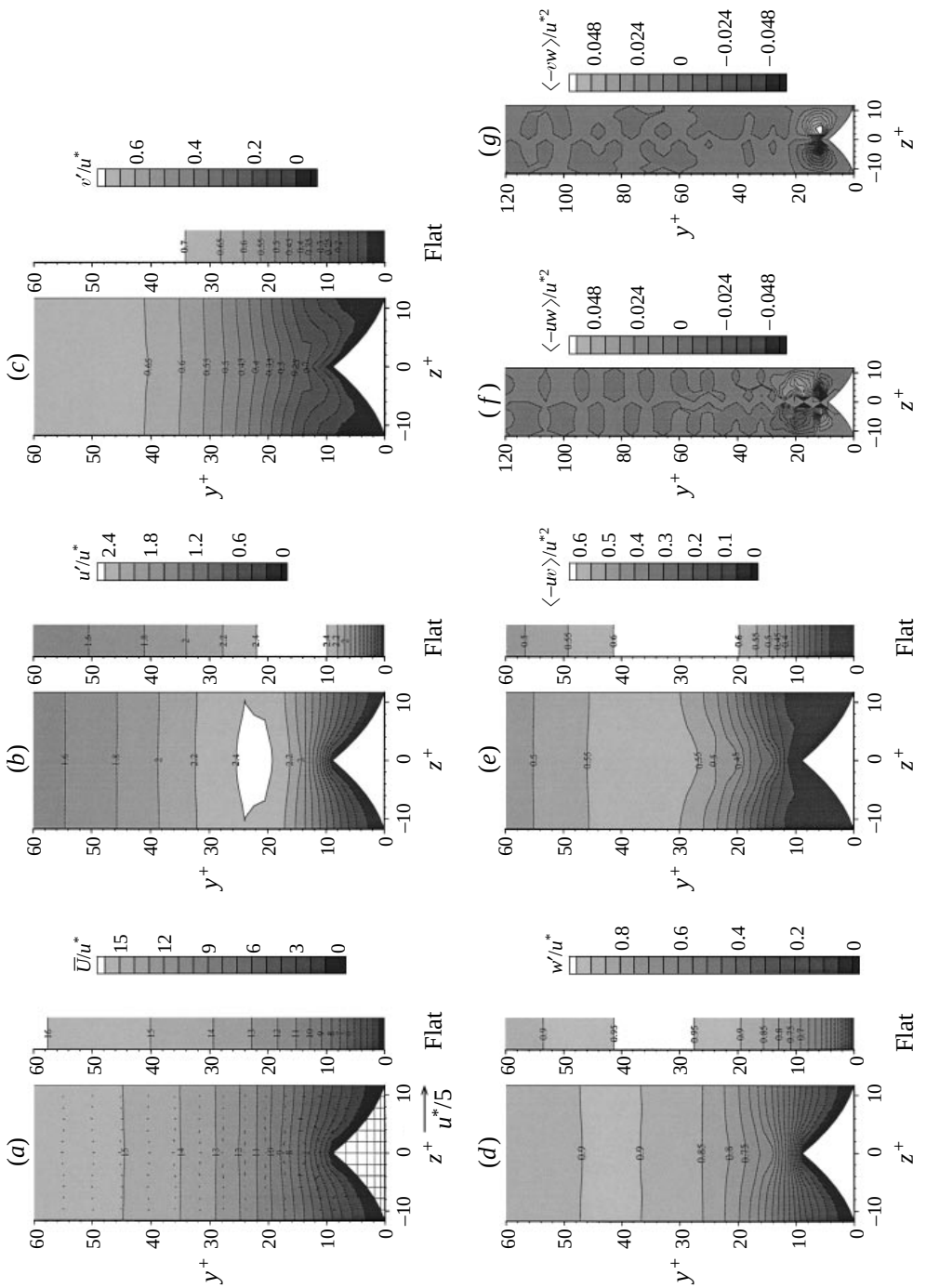

FIGURE 3. For caption see page 124.

valley as has been discussed by nearly every earlier investigator. In figure 3(*b–d*) the turbulence intensities show a general reduction in fluctuating velocities both over the valleys and the crests and that the region of peak fluctuation moves away from the wall. There is a region of particularly small v' values in the riblet valleys as well as a thickening of the region of low u' and w' along nearly the whole riblet surface. We also note that data in figure 3(*a–d*) agree remarkably well with the results for the $S^+ \approx 20$ case of Choi *et al.* (1993). The Reynolds shear stress (figure 3*e*) shows a corresponding reduction in turbulent vertical mixing of streamwise momentum near the riblet (compared to the flat surface), particularly over the valley. The other two Reynolds stresses (figure 3*f, g*) show that in the vicinity of the riblet tip there is a correlation between spanwise motion and both streamwise and wall normal motion. The cause of this correlation is that during a cross-flow fluctuation spanwise flow is deflected up by the windward side of the rib and is thus associated with both upflow and increased streamwise velocity. We will see shortly that figure 3(*f*) and the velocity vectors in figure 3(*a*) suffer from a limited grid resolution.

A quantitative measure of the spanwise length scale defined by the low-speed streaks, λ^+, can be determined by computing the correlation

$$R_{uu}(\Delta z) = \frac{\overline{u(x,y,z)u(x,y,z+\Delta z)}}{u'^2} \tag{3.1}$$

and using the definition that the streak spacing is twice the spanwise distance at which $R_{uu}(\Delta z)$ attains an absolute minimum. The height of this minimum ($y^+_{R_{uu_{min}}}$) is taken as representative of the mean height of the streaks.

The spanwise covariance $R_{uu}(\Delta z)$ is shown at different heights above the walls in figure 4. The streak spacing obtained from the spanwise covariance near both walls is the same: 98.0 for the ribbed side and 99.6 for the smooth side. The height of the streaks above the two walls is different. Over the ribbed wall the covariance minimum occurs at about $y^+ = 20.1$ whereas over the flat wall the minimum occurs $8.1l^*$ lower at $y^+ = 12.0$. Hence, the riblets push the streaks away from the wall by an amount about equal to the height of the riblets themselves. Streak height values are estimated to be accurate to only about $\pm 3l^*$.

For this riblet configuration, experiments (Walsh 1990) indicate only a small 1–5% drag reduction. Our simulation yielded a 3.2% $\pm$1.5% decrease where the error bars indicate a 90% confidence interval assuming a normal distribution for the 24 independent realizations. Hence, the present drag results agree with the experiments.

But are these results sensitive to grid resolution? If the grid resolution is reduced by a factor of two in both the wall normal and spanwise directions with respect to the above nominal case, substantial Gibbs oscillations develop and the solution near the riblets is extremely under-resolved. This might be expected since each riblet would be represented with only 4 grid sites. Near the opposite flat wall, however, the solution remains surprisingly reasonable. On the other hand, if the grid resolution is doubled in both y and z with respect to the nominal case 1 run, the results are seen in

---

FIGURE 3. Mean contours over an $S^+ = 23$, $H^+ = 8.7$ riblet array from a $64 \times 65 \times 128$ simulation (case 1). (*a*) Mean streamwise velocity and velocity vectors. The 3/2's computational grid used for de-aliasing and on which the virtual surface is created is indicated overlaying the riblet. Note the lack of a coherent secondary flow compared to the weak Gibbs oscillation. A vector of length $u^*/5$ is seen below the figure for scale. (*b–d*) Root-mean-square u, v, and w velocities, (*e–g*) negative Reynolds stresses $\langle -uv \rangle$, $\langle -uw \rangle$, and $\langle -vw \rangle$. Shown for comparison are the corresponding mean contours for the opposte flat wall (except for $\langle -uw \rangle$, and $\langle -vw \rangle$ which should be zero).

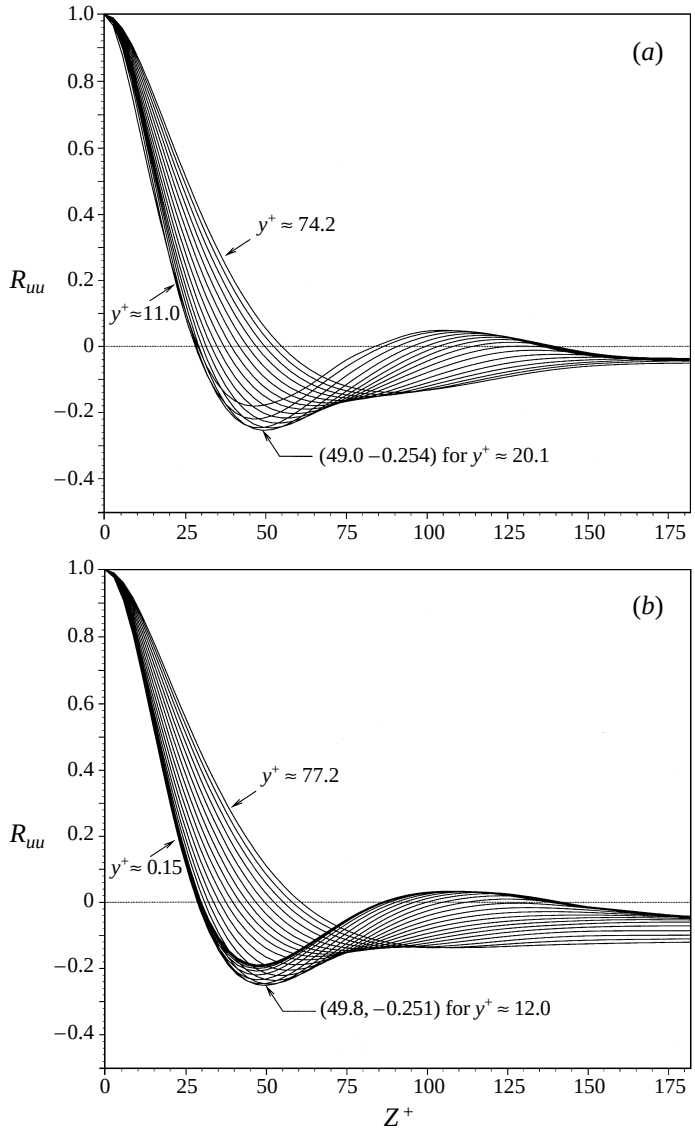

FIGURE 4. $R_{uu}(\Delta z)$ autocorrelation for several different distances from the wall in case 1. (*a*) Near the riblet side. (*b*) Near the smooth side.

figure 5. This simulation, case 2, was run to $T^+ = 7503$ (22 independent realizations) at eight times greater computational expense per realization than for the nominal case. Nonetheless, the results in figure 5 show virtually the same quantitative features as those presented in figure 3. The $\langle -uw \rangle$ contours, which are distorted by the Gibbs oscillations in the low-resolution case, show a clear but weak correlation beside the rib tip in figure 5(*f*). The drag ratio for this higher resolution run is 0.954 ± 0.016 in agreement with the earlier result.

Finally, to prove that case 2 itself is fully resolved we again double the y and z resolution in case 3 (for which the $x:y:z$ resolution is 48:257:512) but can only afford to run to $T^+ = 1903$ (2200 CPU hours on a Cray J90). Nonetheless, the results (not shown) are virtually indistinguishable from those of case 2 – there are no further changes in

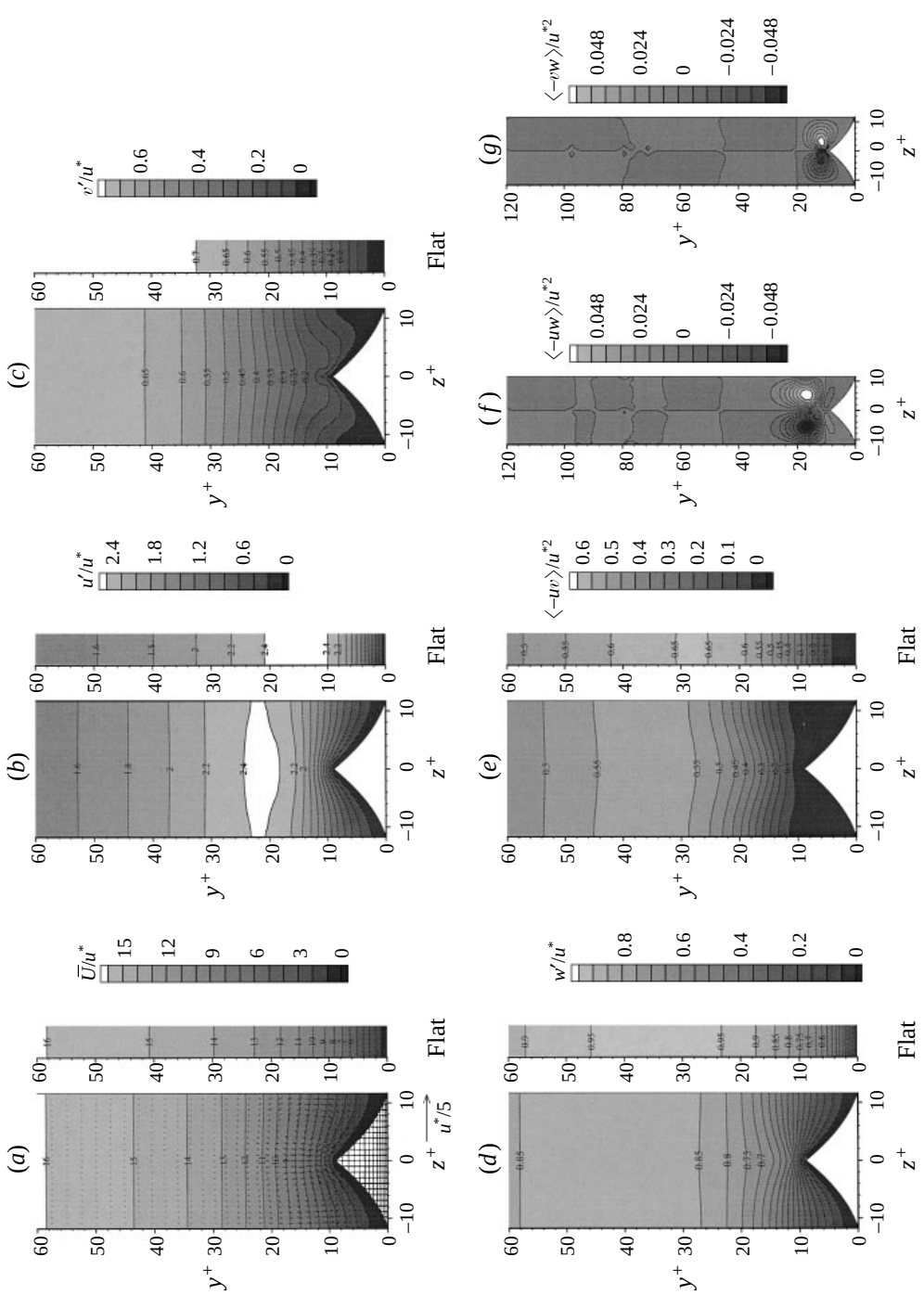

FIGURE 5. Mean contours, as in figure 3, from a $64 \times 129 \times 256$ simulation, case 2. Note the clear secondary flow in (*a*) and the well-defined contours in (*f*).

the velocity vectors or the $\langle -uw \rangle$ contours. Hence, we obtain full grid convergence with a spatial resolution between that of cases 1 and 2. Also, essentially all of the physics is captured by the case 1 resolution except that the weak mean secondary flows (see below) and the small values of $\langle -uw \rangle$ are obscured by the Gibbs oscillations at low resolution. As will be seen later, stronger mean flows are not obscured by Gibbs oscillations and we will choose to utilize the nominal case 1 resolution out of expediency.

Note that in figure 5(*a*) there exists a clear but weak pair of streamwise vortices surrounding the riblet tip. The vortex cores are $4l^*$ above the rib crest and are spaced by $11l^*$. Such vortices cause a weak mean upflow (maximum of $\bar{V}/u^* \approx 0.030$) directly above the riblet crest and a downflow of about the same magnitude over the valley centres. As described above, these vortices are so weak in this closely spaced riblet case that they could not be clearly distinguished from the residual Gibbs oscillations in figure 3(*a*). Choi *et al.* (1993), Suzuki & Kasagi (1994), and Crawford & Karniadakis (1996) also found such weak vortices over their riblets. The vortex pair is clearly visible through time averaging; in animations of the flow one rarely sees a real vortex pair surrounding one of these riblet tips. Rather, there is occasionally an isolated vortex on one side or the other. In §§ 4 and 5 we discuss different physical mechanisms for the creation of such secondary flows. For now, however, we continue with our discussion of the effects of varying riblet spacing.

3.2. *Drag increasing configuration*

Next consider what happens as the spacing between riblets is increased to $S^+ = 62.8$ in case 4. The riblet shape and H^+ are held fixed: the flat region in the valleys is simply made larger thereby permitting only 6 riblets in the channel. The simulation parameters are otherwise the same as case 1. The crest-to-crest rib spacing is chosen to be slightly larger than the mean vortex spacing in a flat-plate boundary layer.

Figure 6 presents data corresponding to those in figures 3 and 5. There is again a clear arching up of the mean streamwise velocity contours over the riblet crest (figure 6*a*). What is also immediately obvious is that there is greater turbulent activity (figure 6*b–d*) over these more widely spaced riblets as revealed in the turbulence intensity contours. The shapes of the contours show a remarkable similarity to those of the $S^+ \approx 40$ large 60° riblets of Choi *et al.* (1993) (their figure 12*a*). The regions of reduced turbulence very close to the riblet surface are perceptibly thinner in figure 6 than in figure 5. The turbulence intensities appear to almost recover the smooth wall profile in the valley midway between adjacent riblets. There is an increase in Reynolds shear stress (figure 6*e*) over the riblet and a small region of low $\langle -uv \rangle$ on the riblet flanks. The other two Reynolds stresses (figure 6*f, g*) are two to four times greater than in the previous case and again show that in the vicinity of the riblet tip there is a correlation between spanwise motion and both streamwise and wall normal motion.

As others have found (Walsh 1990) there is an increased skin friction drag in comparison to the flat-plate case: $DR = 1.04 \pm 0.02$. The vectors of figure 6(*a*) show a fairly large and strong pair of secondary vortices; the peak vertical velocity, $\bar{V}/u^* \approx 0.12u^*$, is more than three times that found in figure 5. These vortices convect low-speed fluid along the riblet surface up over the riblet crest and bring high-speed fluid down toward the wall on either side of the riblet. The region of upflow is clearly associated with increased levels of u' and $\langle -uv \rangle$. While this mean vortex flow is only an ensemble average of various flow field realizations, in animations one does find the tendency for a pair of streamwise vortices to occasionally hover around the riblet crests. This case 4 is in a sense transitional between closely coupled riblets (cases 1–3) and isolated riblets (cases 5 and 6, below).

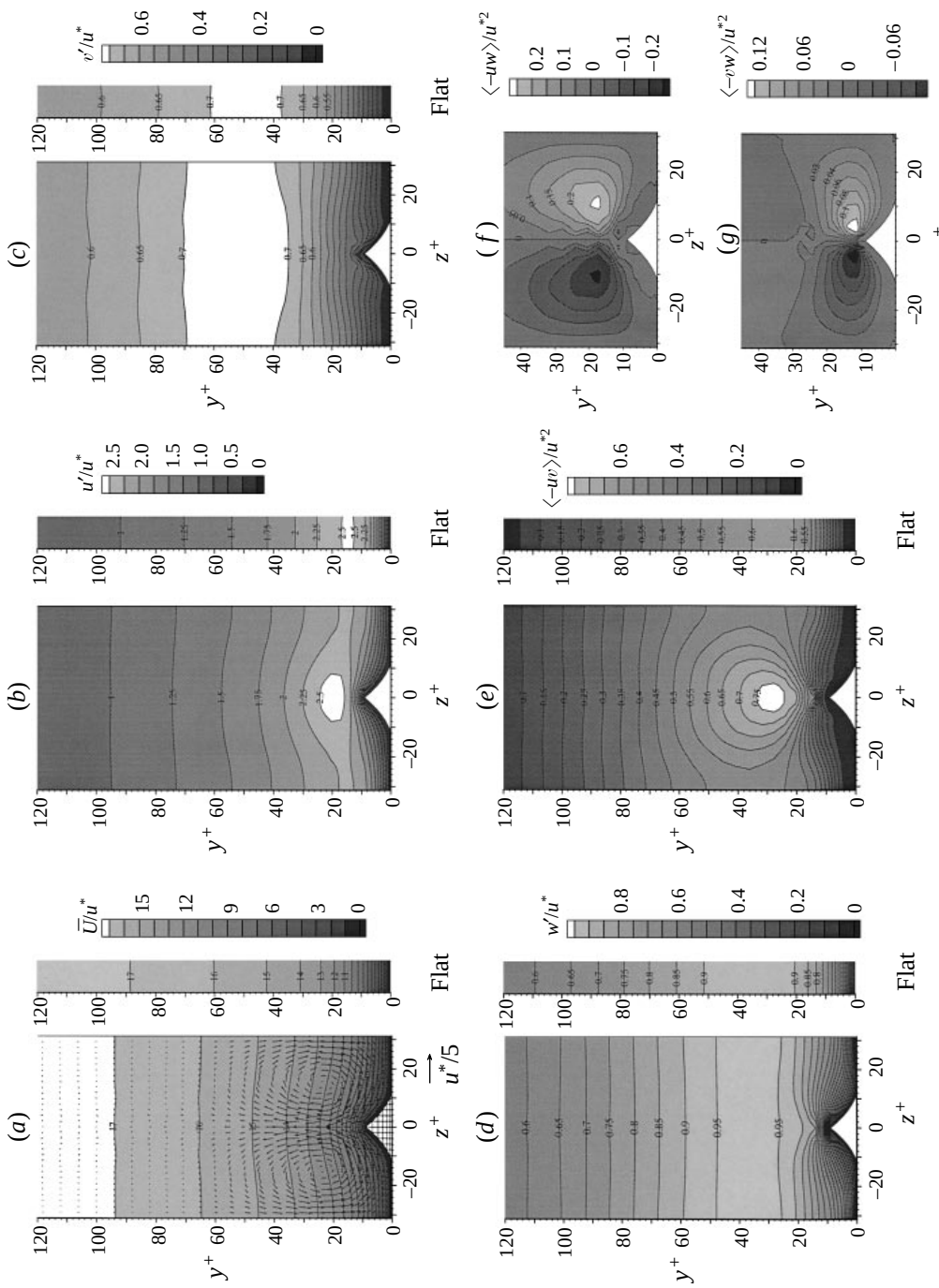

FIGURE 6. Mean contours, as in figure 3, for $S^+ = 62.8$, case 4. Note the different grey scales than in figure 3.

That the riblet crest spacing was set slightly larger than the mean vortex spacing in a flat-plate boundary layer did not seem to force the vortex spacing to become synchronized with crest spacing. That is, the mean streak spacing did not rise to 125.

3.3. *Isolated Riblet*

Finally, consider a simulation at nominal resolution of a single riblet along the lower wall of the channel in case 5. Since the flow is periodic in z this is not a truly isolated riblet but rather represents riblets having a crest-to-crest spacing equal to the box width, $375l^*$. Similar trends are seen in figure 7 as were found over the $S^+ = 62.8$ riblets. Root-mean-square fluctuations are enhanced both above the riblet and $\approx 2H^+$ to either side. There continues to be a region of decreased $\langle uv \rangle$ directly on the riblet flanks but an enhanced region over the crest. One sees, moreover, that the mean contours return to the flat-wall values about 60–80 wall units to either side of the riblet thereby delineating the spanwise extent of influence. That is, this $H^+ = 8.9$ riblet is effectively isolated. Also, the vortex pair, at least over widely spaced riblets, appears to be due to the influence solely of the riblet which the pair hovers above and not to some cumulative effect of interacting riblets. The secondary flow associated with the riblet is strong ($\bar{V}/u^* \approx 0.32u^*$). The regions of downwash are associated with diminished velocity fluctuations and shear stress while upwash is associated with increased velocity fluctuations and shear stress. There is only a slight increase in viscous drag in comparison to the flat-plate case: $DR = 1.012 \pm 0.011$. This is as expected: as small riblets are spaced more widely they influence less of the plate surface and the drag ratio should return to 1.0.

This configuration was also used to check the grid resolution. In figure 8 are presented the results from a run (case 6) made at double the nominal resolution in the spanwise and wall normal directions. The various quantities are nearly the same within a distance of $\approx 8H^+$ to either side of the riblet where the influence of secondary flow is the greatest. However, at this higher resolution it appears that there are other weaker *tertiary* vortices which occur further from the riblet at about $\pm 95l^*$ and even $\pm 155l^*$. Even with the lower resolution in case 5 very weak tertiary vortices are seen but they lie mostly beneath the main secondary pair. We note that while case 5 was run for a long time ($T^+ = 15\,660$), it was only possible to run case 6 for half as long. Hence, case 6 still shows vestigial effects of ordinary streamwise vortices on the opposite flat wall which are not much weaker than the tertiary flow. In that the tertiary vortices in case 6 appear to weaken somewhat when a larger number of realizations are averaged, it appears that there is probably little effect of resolution upon tertiary flow.

4. Turbulent flow over isolated elements

We have just seen that as the spacing between riblets increases four things of interest occur: (i) the drag benefit of the riblets disappears, (ii) the turbulent activity near and above the riblet increases, (iii) the secondary flow becomes much stronger with the vortex cores rising higher and spreading apart, and (iv) tertiary flows may occur. We suggest that the secondary flows are both indicative of and the cause of the reduced performance of the widely spaced riblets. To see why, one must investigate what causes the secondary flow. This section presents the results of simulations of turbulent flow over three different types of longitudinal elements to isolate which features of a riblet are most responsible for secondary flow. The next section (§5) will present a two-dimensional flow model (in the y, z-plane) to explain many of the phenomena observed in the full turbulent simulations.

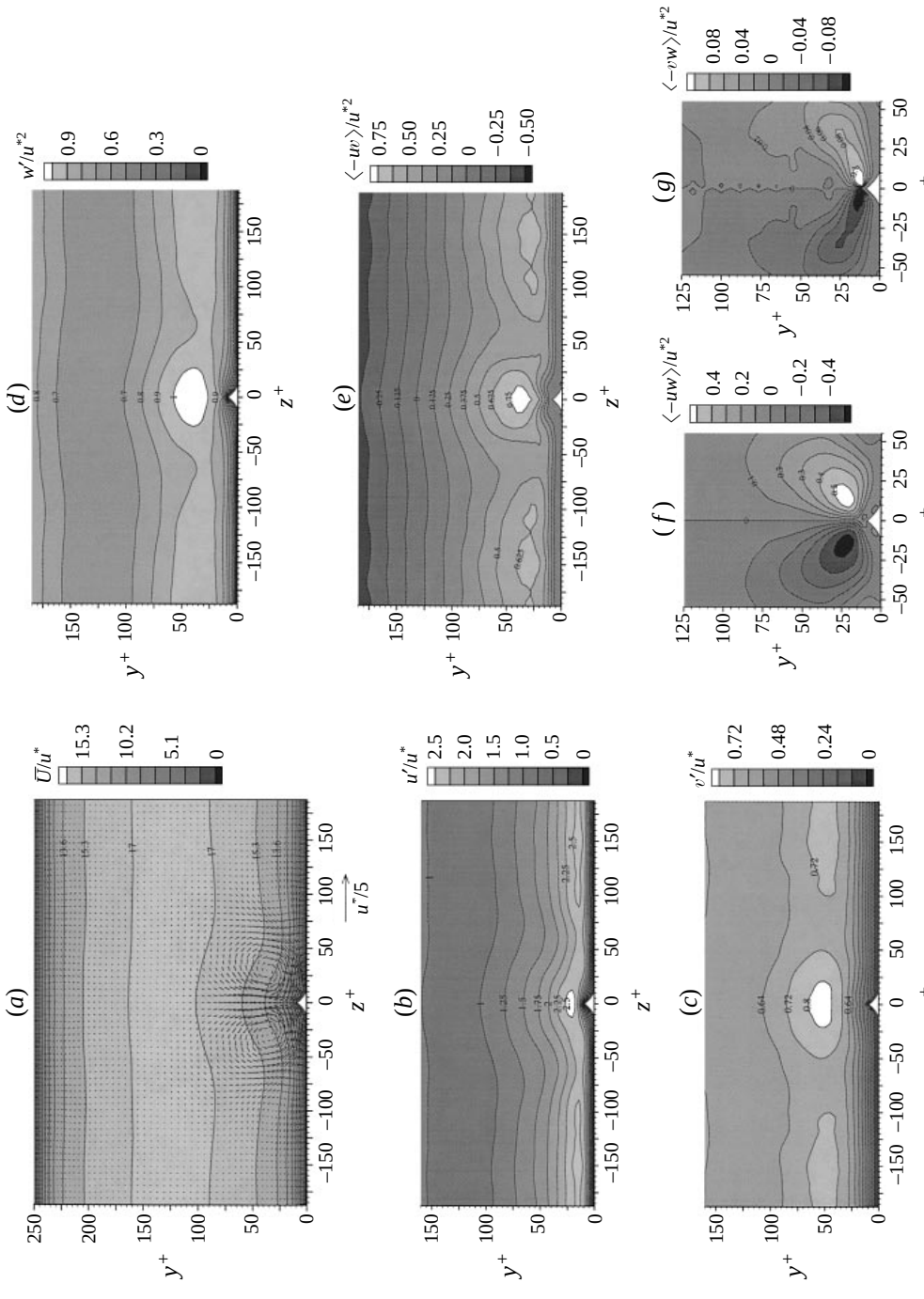

FIGURE 7. Mean contours of turbulent flow over an $S^+ = 375$ riblet, case 5. Flow over the opposite flat wall is not shown in every figure but the full field is seen in (*a*). Again, note the different grey scales from the previous figures. Also, the length of the velocity vector shown below (*a*) is now u^*.

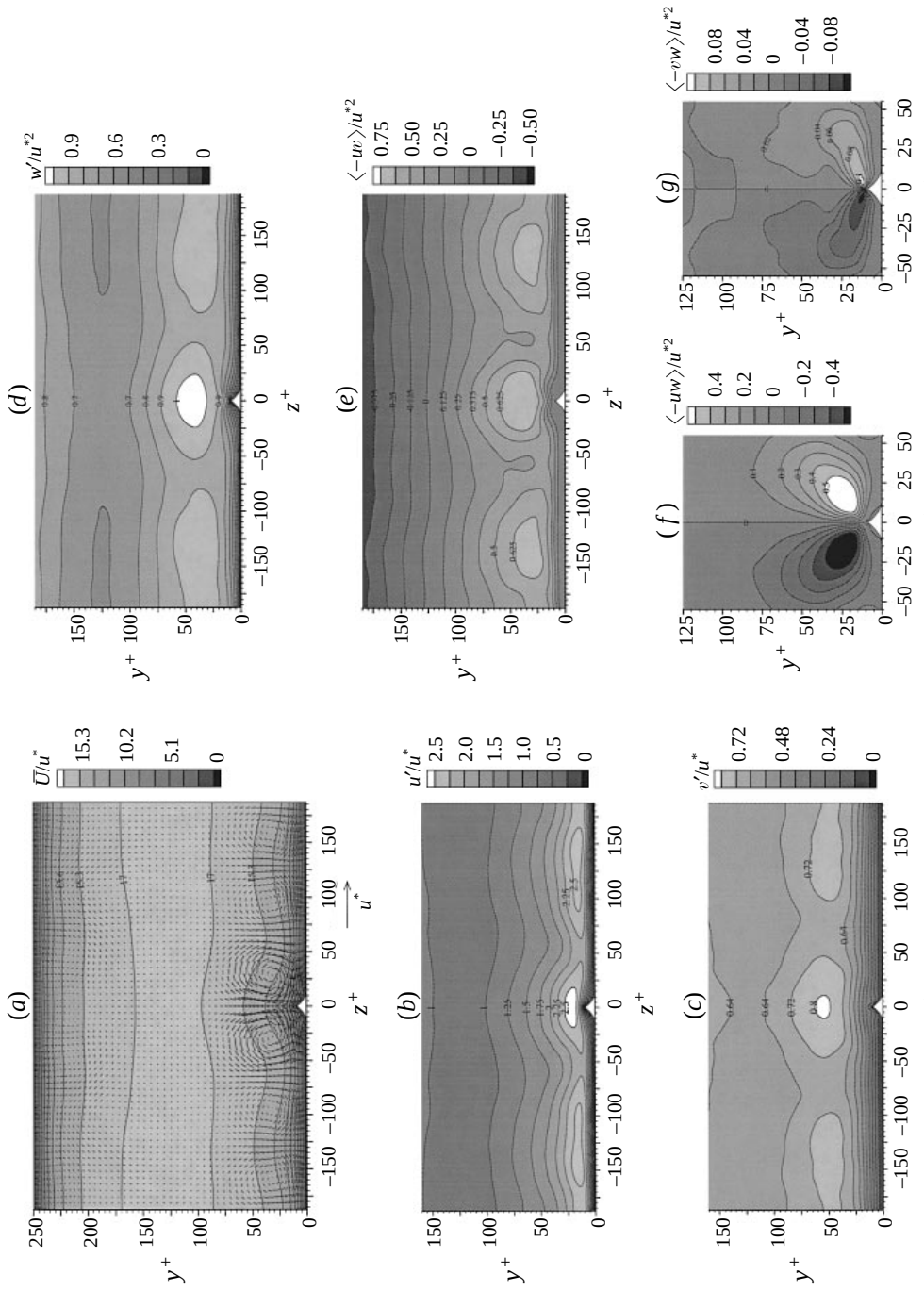

FIGURE 8. Same as figure 7 except that the grid resolution is doubled in the y- and z-directions, case 6. Note although there is a clear tertiary flow, it is comparable in strength to the vortices near the top wall and longer time integration would be desirable.

Consider the different ways one can view what a riblet does. Riblets can either be thought of as a set of slots incised in a surface or as ridges projecting from a surface. Section 3 examined the effect of an isolated longitudinal ridge on a turbulent flow. Section 4.1 will consider the effect of an isolated slot on such a flow with particular attention being paid to the nature of any associated secondary flows. Another way to view a riblet is to note that much of its influence on the flow well above the wall comes from the very crest of the ridge. Section 4.2 will investigate the nature of the crest influence by replacing a whole riblet with a single wire where the crest would have been. Section 4.3 first shows that a vertical fin produces nearly the same results as a riblet. Then, to answer the question as to the physical cause of the secondary flow, a vertical fin is modelled which provides no through-flow in z but allows velocity slip in the y- and x-directions.

4.1. *Turbulent flow along isolated slots*

Consider flow along the length of a single slot ($9.2l^*$ deep and $27l^*$ wide) having a smooth contour like that of a riblet valley in cases 1–3. The slot is created in the same manner as the riblets by applying the force field along a sequence of grid sites near the lower channel boundary. Other simulation parameters are presented in table 1 for this case 8.

Figure 9 provides contours of several x-averaged properties over the slot along with velocity vectors in the (y, z)-plane. The flow in the slot is slow. While the Reynolds shear stress is low, the other two Reynolds stresses show clear but weak maxima and minima near the lips of the slot. The reason appears to be simply that when there is a local positive w fluctuation, near the left lip fluid pours down into the slot while near the right lip it flows up and out. Hence, in explanation of the $\langle -vw \rangle$ trends, there is a correlation between positive w fluctuations and $-v$ fluctuations on the left and $+v$ fluctuations on the right. A similar argument applies to negative w fluctuations and similar reasoning explains the $\langle -uw \rangle$ contours. As seen in figure 9(d) spanwise fluctuations clearly do penetrate into the valley. There is a region of diminished v' on the valley floor that is similar to that found in figures 3(c) and 5(c).

If we double the spatial resolution in y and z (case 9), figure 10 illustrates that the contours are not much affected. In both cases 8 and 9 one finds weak secondary and tertiary flows. In particular, in case 9 there is a secondary flow which is down into the valley of the slot and out along the flanks very much like what occurs in the riblet valleys of cases 2 and 3. No such secondary flow within the slot is discernible for case 8 due to the Gibbs oscillations.

Case 8 shows one other vortex pair at a large distance from the slot as well. However, in that these runs were not long (to $T^+ = 16\,198$ for case 8 and $T^+ = 6767$ for case 9) and the tertiary flows are weak (of comparable strength to the vestiges of ordinary buffer layer vortices seen on the opposing flat walls), no definite conclusions can be drawn about the nature of these tertiary flows.

It is not surprising that with so little effect of the slot on the mean flow features, the drag on the slotted plate is virtually the same as on the flat wall and that the streak spacing and height are unaffected (table 1). The results found for a smaller slot (case 7, not shown) are generally similar (see table 1). Thus, we find that an isolated slot used to model a riblet valley probably does induce a secondary flow comparable to that over the valleys of closely spaced riblets. The slot also shows evidence in the $\langle -uw \rangle$ and $\langle -vw \rangle$ contours of the effects of a low-Reynolds-number spanwise sloshing motion.

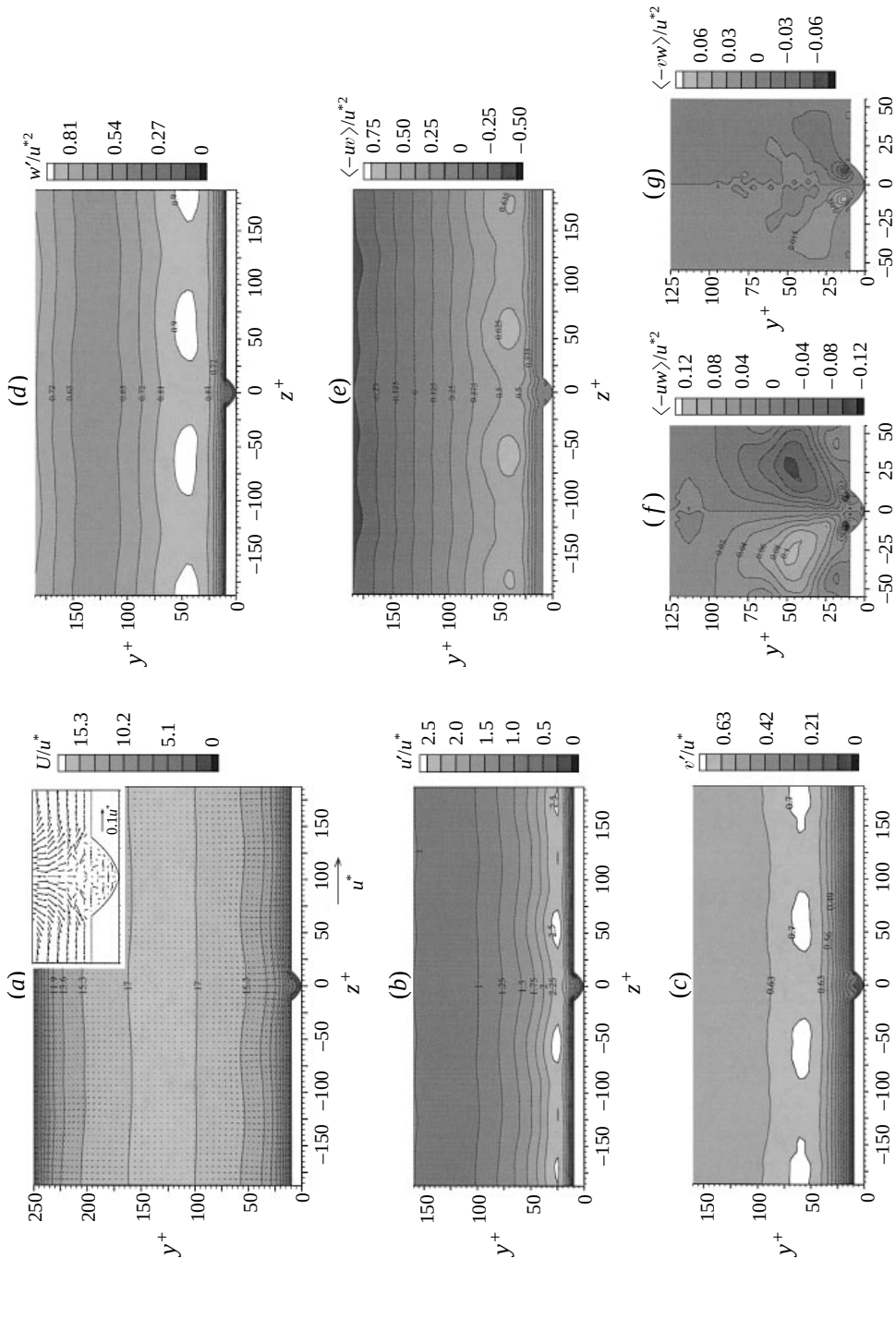

FIGURE 9. Mean contours over a single slot, case 8. (*a*) Mean streamwise velocity and velocity vectors. (*b–d*) Root-mean-square u, v, and w velocities; (*e–g*) Reynolds stresses $\langle uv \rangle$, $\langle uw \rangle$, and $\langle vw \rangle$.

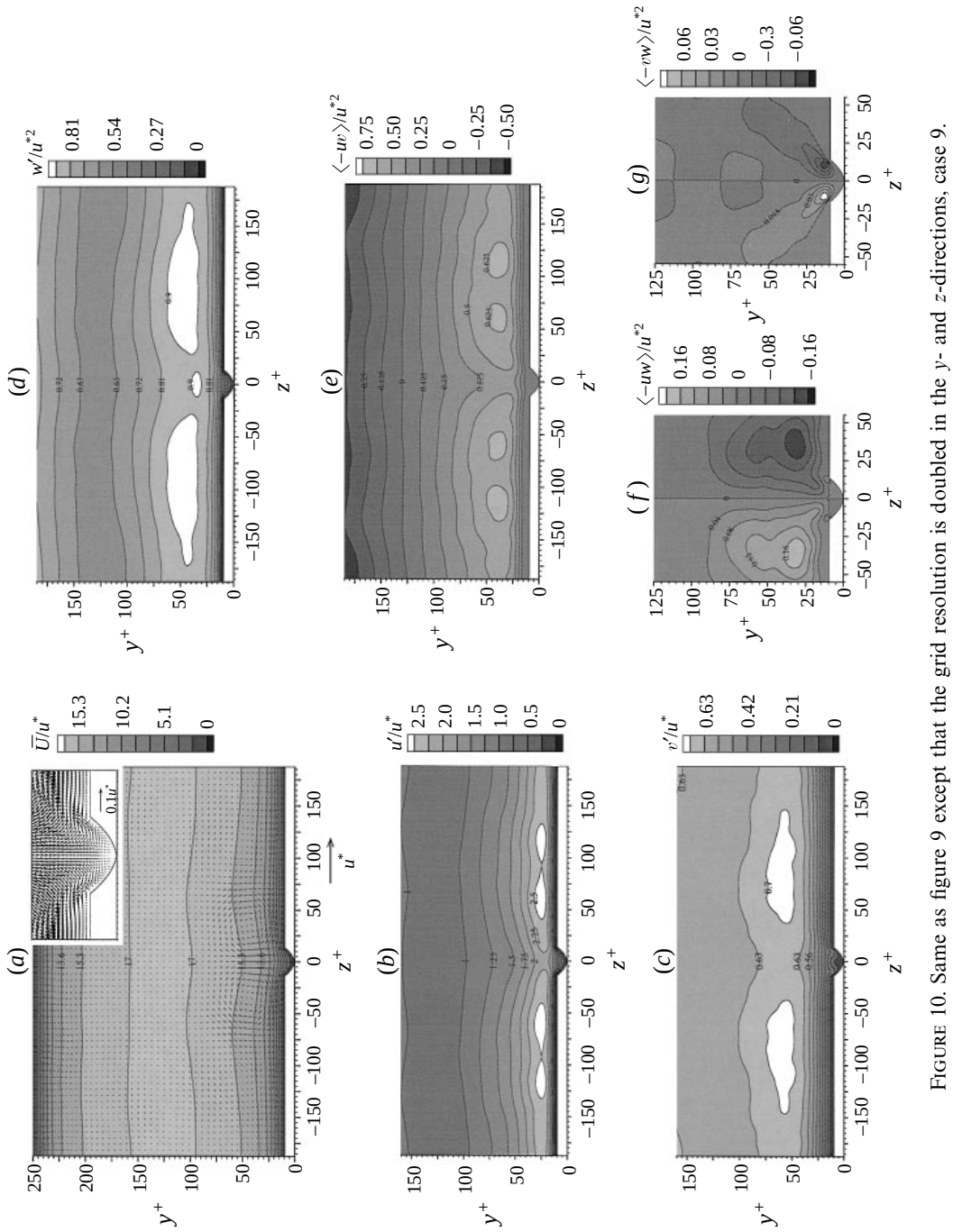

FIGURE 10. Same as figure 9 except that the grid resolution is doubled in the y- and z-directions, case 9.

4.2. *Turbulent flow along isolated wires*

Next consider the effect of placing a single streamwise fine wire just above a flat plate in a turbulent boundary layer. This is analogous to modelling the effect of an isolated riblet crest. Kramer (1937) suggested that many such longitudinal wires could shield the plate from turbulent fluctuations and Bechert *et al.* (1997*a*) tested such an idea but found mostly a drag increase. Goldstein *et al.* (1995) presented results from a simulation of Kramer's idea which showed that for one configuration of multiple wires ($S^+ = 40.5$ and $H^+ = 5.5$) fluctuations below the wires were indeed reduced. However, fluctuations over the wires were increased as was the net drag on the wires/flat surface. Above the wires the various mean profiles resembled the same profiles taken over a corresponding riblet array. Goldstein *et al.* (1995) concluded that the effects found indicate that widely spaced wires deflect cross-flow both up and down – above and below the wire.

We will consider turbulent flow over isolated wires with heights of $H^+ = 9.2$ and 15.3 (9th and 11th grid sites above the wall for cases 10 and 11, respectively). The flow domain size and resolution are initially the same as were used in case 5. The top and bottom flow boundaries are ordinary no-slip surfaces. The wires are created with the force field technique simply by applying the body force to a string of grid sites where the wire is desired. The force field is interpolated to the grid sites with a narrow Gaussian distribution (ϵ in table 1). Thus, the effective width of the wire is about two grid sites or about $4l^*$.

Figures 11 and 12 present some remarkable results. Over both wires one again finds the secondary flow like that found over the single riblet: a vortex pair surrounding the element creating upwash directly over the wire and downwash on either side. One finds, however, that there is also now a much larger tertiary vortex pair of opposite sign surrounding the original secondary vortex pair. The vortex structures near the $H^+ = 9.2$ wire are very similar to those near the $H^+ = 8.9$ riblet. The tertiary flow appears to restrict the development of the secondary pair, particularly for case 11 in which the tertiary pair becomes huge (figure 12*a*). Above the wire, in the region of upwash of the secondary flow, there are large turbulent fluctuations. On the other hand, the fluctuations seem reduced in the regions between secondary and tertiary vortices where the flow is down toward the plate. The Reynolds shear stress, $\langle -uv \rangle$, is enhanced in a mushroom-shaped region above the wire, a region closely associated with the secondary vortex pair alone. The other two Reynolds stresses also show clear patterns linked only to the secondary flow: $\langle -uw \rangle$ has a dipolar pattern while $\langle -vw \rangle$ appears predominantly dipolar with some quadrupolar nature due to two smaller lobes below the wire. The large dipolar $\langle -uw \rangle$ pattern seen about the $H^+ = 9.2$ wire seems squashed down by the much stronger tertiary flow near the $H^+ = 15.3$ wire. There do not appear to be other appreciably enhanced regions of Reynolds stress associated with upflow in the tertiary vortex pair.

All of these patterns agree remarkably well with those found for the single isolated riblet (case 5) except for the presence of the particularly prominent tertiary mean flow. This agreement, notably between similarly sized cases 5 and 10, appears to confirm the idea that a wire can be used to model many of the effects of a riblet and that most of the effect of an isolated riblet comes from the riblet crest.

The mean streamwise velocity contours in figures 11(*a*) and 12(*a*) show a thickening of the boundary layer over the wire but it is not clear if this is simply due to the no-slip wire projecting into the flow or due to the secondary vortex pair upwash. There is, however, a clear effect due to the tertiary vortex pair: the boundary layer

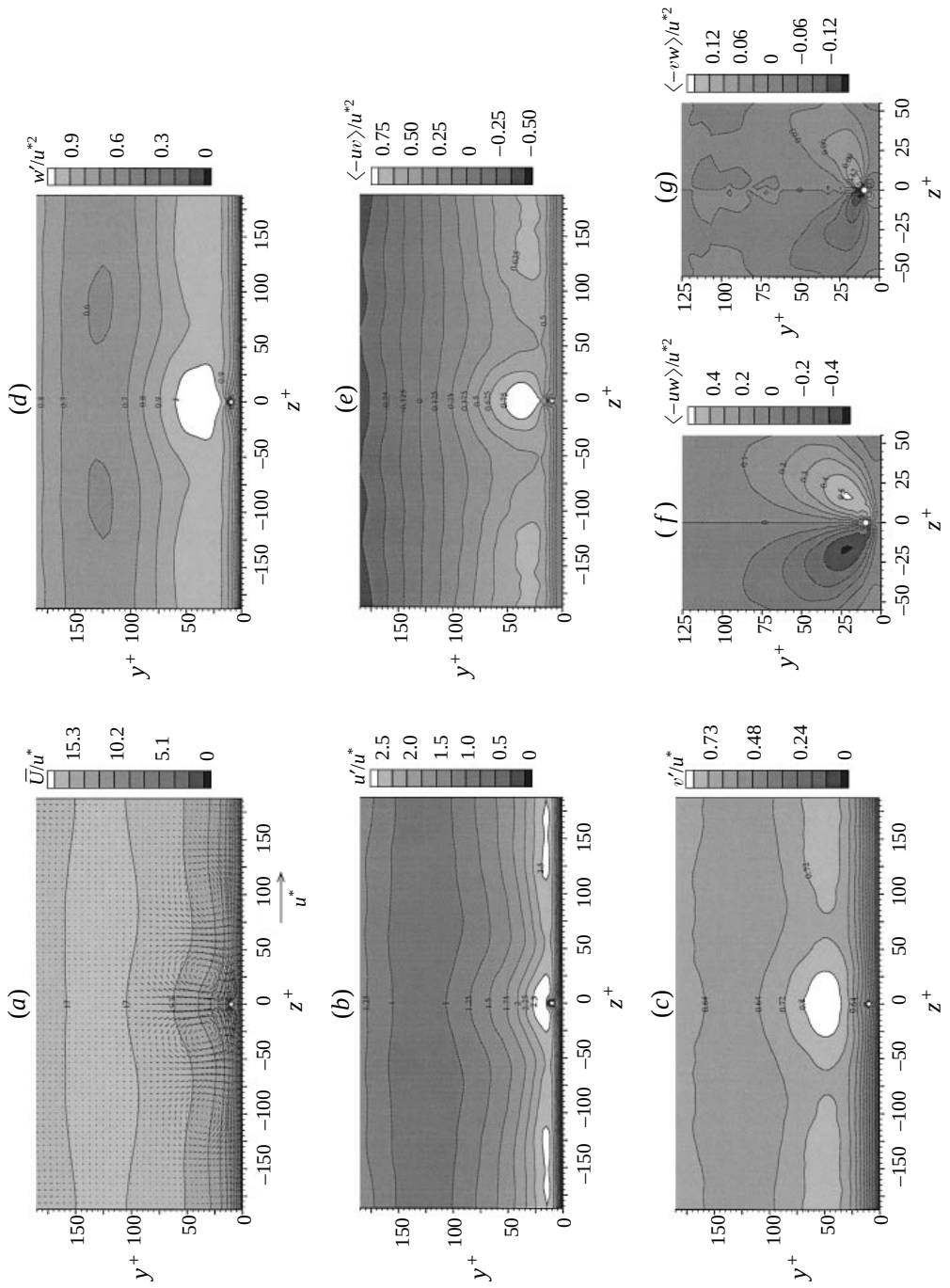

FIGURE 11. Mean contours over a single wire at $H^+ = 9.2$ for case 10. Contours as in figure 9. Particularly note the large tertiary flows.

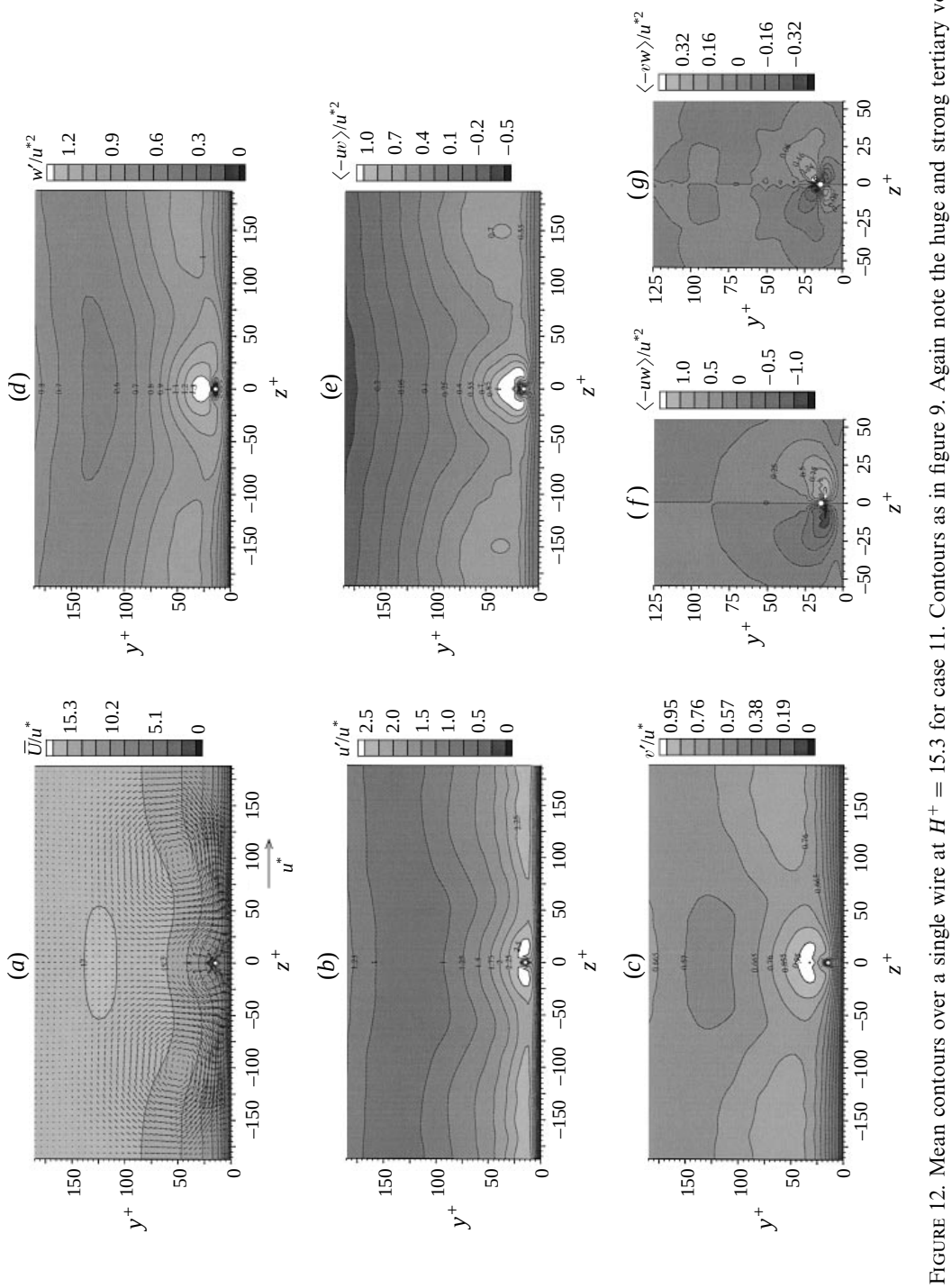

FIGURE 12. Mean contours over a single wire at $H^+ = 15.3$ for case 11. Contours as in figure 9. Again note the huge and strong tertiary vortices.

is thickened in regions of mean upwash and thinned in regions of downwash. The mean drag of the wire/wall is increased by $4.5 \pm 1.5\%$ and $19.4 \pm 3.4\%$ for the low and high wires, respectively.

But are such large tertiary vortices reasonably modelled in a box of a span only slightly wider than the vortices themselves? And what about the adequacy of the spatial resolution? To address these questions we re-ran these two simulations with the width of the box (L_z) increased by 66%. The number of grid cells was held constant so that the resolution of the flow was reduced by 66% in the z-direction. As seen in the case 12 and 13 data in table 1, the secondary and tertiary flows are nearly the same as those found in the narrower domain. In fact, all of the various contoured mean properties (not shown) are virtually unchanged by the change in domain size. The differences observed are minor and are felt to be due to insufficient statistical sampling to fully capture a weak secondary flow. One concludes that the boxes used are sufficiently large and the resolution is probably adequate to capture the physics discussed.

4.3. *Turbulent flow along isolated fins: what causes secondary flow?*

Secondary flows have thus been found to be associated with isolated riblets and wires which project well into the viscous sublayer but are weak in slots which are submerged below the mean sublayer height. Additionally, the secondary flow vortices appear strongly associated with enhanced turbulent activity. But what causes these vortices? It may be that tilting of the mean vorticity components Ω_y and Ω_z along the sides of the riblet or wire by the mean shear ($\Omega_y \partial \overline{U}/\partial y + \Omega_z \partial \overline{U}/\partial z$) produces the streamwise secondary vortices, and the mean shear and vorticity in a single slot valley is too low (or the two terms nearly cancel) to cause strong vortices. Or perhaps the vortices are Prandtl's secondary flow of the second kind found in turbulent flow through channels of non-circular cross-section. In the classic corner flow problem the interaction of the Reynolds stresses with the distorted mean isotachs is thought to cause the secondary flow. The mechanisms producing such secondary flows were reviewed by Demuren & Rodi (1984) and Gessner (1973) and investigated with DNS by Huser & Biringen (1993). We will propose a numerical experiment to provide a useful alternative physical explanation of such flows.

Consider first the turbulent flow along a vertical fin (case 14), a situation very much like that of flow along a taller case 5 riblet. The fin is created as was the riblet: the force field is applied to bring the flow to rest on a sheet of grid points at $y^+ = 14.4$ and below. As before, the force field has a narrow spatial Gaussian distribution so the effective width of the fin is about two grid sites or about $4l^*$. All of the contours (figure 13) are very much the same as those over a single riblet. A fairly strong secondary flow is also found (figure 13*a*). The calculation was done in a box having a width like that used in the wide-box wire simulations (width = $600l^*$) yet no tertiary flows are seen which are clearly distinct from the vestiges of the ordinary buffer layer vortices. A much longer run would be required to clarify any weak tertiary flow. The main point is that the fin can be viewed as a riblet of nearly zero width.

Suppose we consider a fin of the same size but instead of making it a no-slip surface we permit fluid to slip in the x- and y-directions (case 15). The force field is only applied in the z-direction in order to prevent flow through the fin and would deflect spanwise flow up over the fin. Such a surface does not generate vertical vorticity (Ω_y) along its sides which can be tilted into the x-direction. The surface also does not retard the streamwise velocity so in a laminar flow the streamwise velocity contours

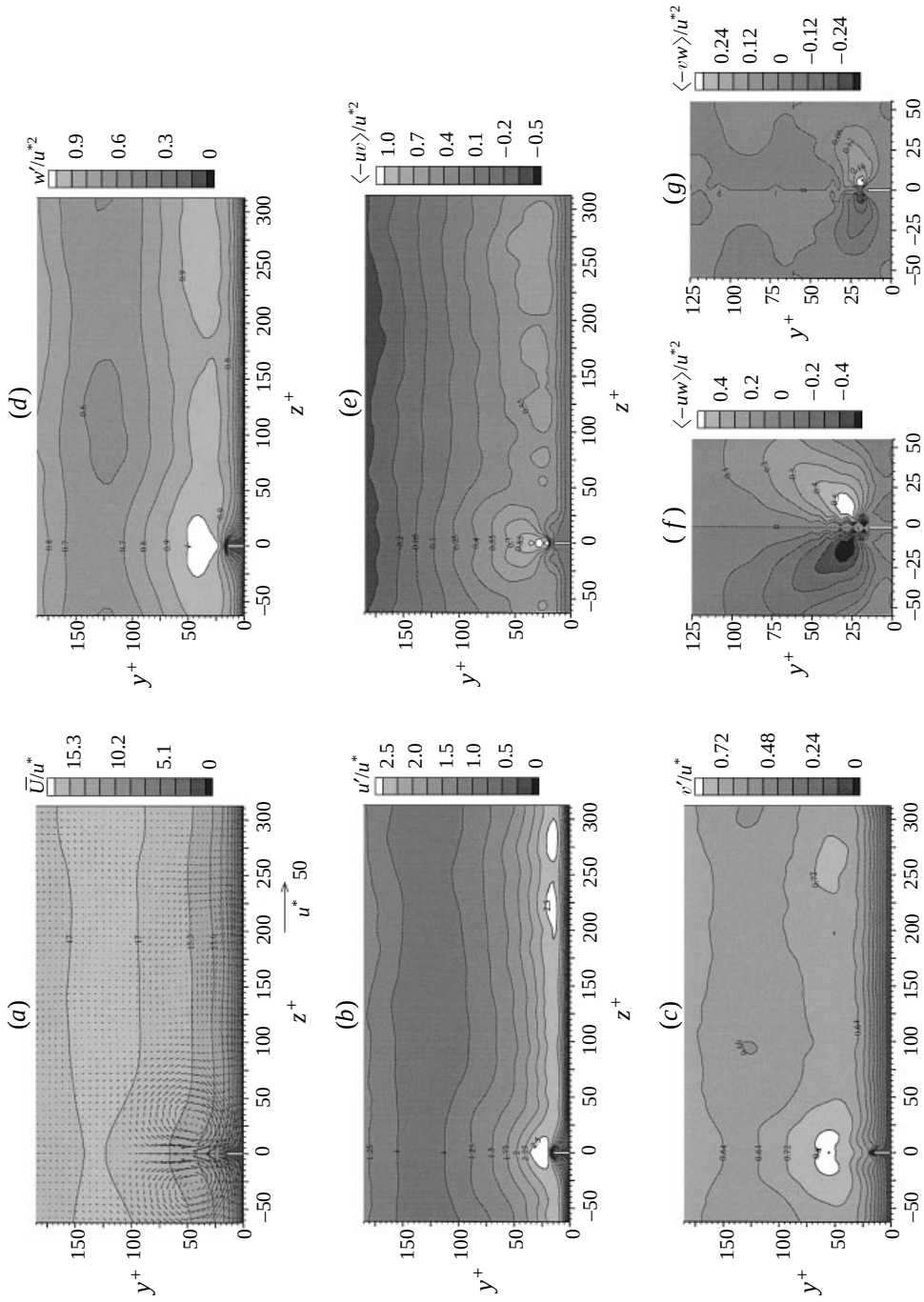

FIGURE 13. Mean contours over a single fin $14.4l^*$ high, case 14. Contours as in figure 9 in an offset domain for clarity. Notice the strong similarity to the results presented in figure 7.

would remain flat and continuous right through the fin. There would thus be no tilting of the spanwise vorticity (Ω_z) along the fin since the mean shear stress $\partial\overline{U}/\partial z$ would be zero. Hence, the vortex tilting mechanism would not apply. Similarly, a secondary flow mechanism associated with a distortion of the primary stress field is not possible. The damping fin does not produce the mean primary flow which can be used, as Prandtl did, to explain secondary flow of the second kind.

Yet, figure 14 shows that this w-damping fin produces a secondary flow which is, in fact, stronger than that over the regular fin as measured by $\bar{V}_{max}/u^*$ (table 1). The streamwise and wall-normal r.m.s. velocities are little different from those of figure 13 except very close to the fin. The w' contours look almost the same over the two types of fins. It is important to note that over the w-damping fin the streamwise velocity contours in figure 14(a) arch up much as they did over the regular fin. That is, in this case the secondary flow is causing the distortion of the primary flow isotachs rather than the other way around.

So then what does cause the secondary and tertiary flows? First, recall that closely spaced riblets produce nearly negligible secondary flows and that such riblets can produce their drag-reducing effect by damping cross-flow fluctuations (Goldstein *et al.* 1995). As riblets of fixed size are spaced more widely, they are probably less effective in damping w fluctuations; the cross-flow can penetrate into the valleys and then wash over the next riblet. Many of the effects of a riblet, including the formation of secondary flows, come from the riblet crest rather than the valley or the no-slip/no-through-flow condition. And, from figure 14, it appears that the only feature needed for secondary flow to occur is that there are some w fluctuations and that the element, whatever it is, can damp the fluctuations and deflect them vertically. Thus, the mechanism we are looking for may be a strictly two-dimensional phenomenon in the (y, z)-plane.

5. Two-dimensional mechanism of secondary flows

We propose that the secondary flows are caused by the upward deflection of spanwise fluctuations and perhaps by flow separation. In a turbulent boundary layer there will be spanwise fluctuations having a range of frequencies and amplitudes caused by the various flow structures buffeting the near-wall region. The character of the spanwise flow is indicated by a Reynolds number based on a representative cross-flow velocity and the height of the element and a Strouhal number based on a representative frequency. If the perturbations are strong (or simply the riblet is truly sharp), the cross-flow can separate and the shed Ω_x vorticity will roll up into a concentrated vortex on the leeward side of the riblet while the flow on the windward side is still attached and smooth. Positive and negative fluctuations are equally likely. During a $-w$ fluctuation there will be $-\Omega_x$ oriented vortices on the left-hand side of the riblet and during a $+w$ fluctuation $+\Omega_x$ vortices on the right-hand side. Both vortices create upwash over the riblet crest and a time average of the situation would show the presence of a mean secondary flow.

Even at low Reynolds number the cross-flow produces a concentrated outflux of Ω_x near the riblet tip where the tangential surface pressure gradient is large and

† Prandtl also later wrote, in reference to secondary flow in turbulent flow in channels of non-circular cross section: 'The observed facts, however, justify the idea that at places where the shearing stress at the boundary is greater, fluid is impelled toward the centre of the channel as a result of turbulence, and on the other hand at places where the shearing stress is less (e.g. at the corners), fluid flows from the inside towards the wall' (Prandtl 1952, p. 149).

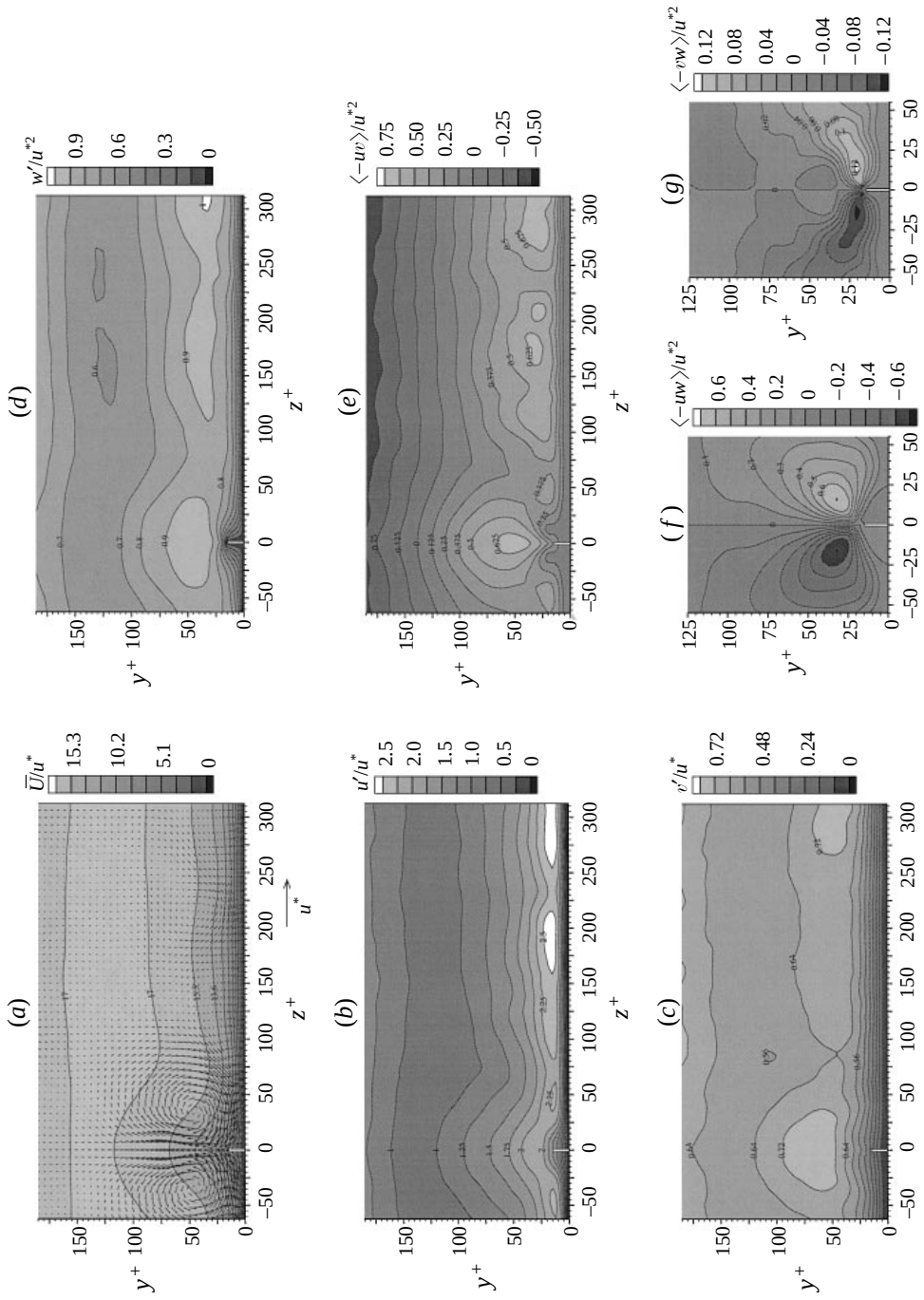

FIGURE 14. Mean contours over a single damping fin $14.4l^*$ high, case 15. Contours as in figure 9 in an offset domain for clarity. The body force is only applied in the z-direction. Strong secondary flows are seen.

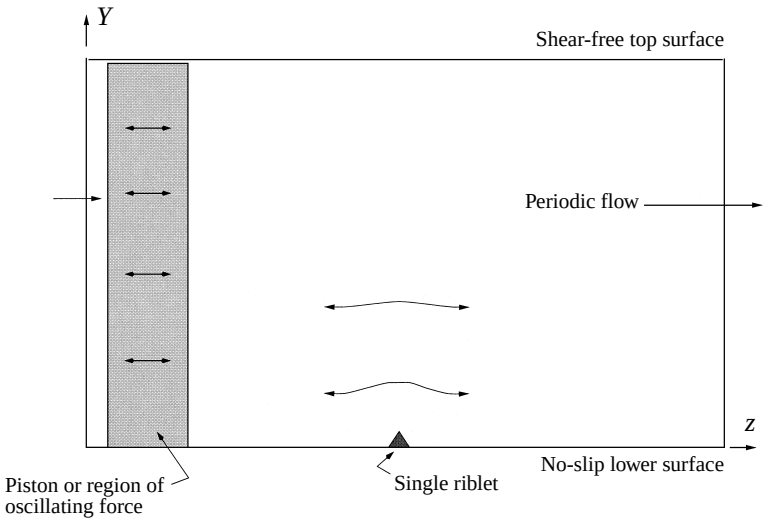

FIGURE 15. Schematic view of the numerical simulation of piston-driven two-dimensional flow.

this vorticity can then diffuse and convect (but not clearly separate) into the flow. The time average of the oscillating flow would show the presence of mean vorticity concentrations on either side of the riblet.

5.1. *Sinusoidal spanwise motion*

We can test these ideas with the following numerical experiment. Consider a two-dimensional domain analogous to a single (y, z)-plane from a turbulent simulation. A single element is placed on the lower surface and a uniform oscillating flow in the z-direction is driven by a piston on one side of the domain. The flow is periodic (Fourier) in the z-direction and the piston is created with the force field simply by specifying the desired piston velocity in several columns of cells far from the element (Goldstein, Adachi & Izumi 1993*a*). The situation is represented schematically in figure 15. For sinusoidal oscillations the piston velocity, $w_{pist}(t)$, is characterized by a specified maximum amplitude, w_{max}, and frequency, ω: $w_{pist}(t) = w_{max}\ \sin(\omega t)$. We define an element Reynolds number by $Re_e = w_{rms}h/\nu$ and a Strouhal number by $St = \omega h/w_{rms}$, where w_{rms} is the root-mean-square spanwise sloshing velocity. The Stokes layer on the flat wall has a 99% thickness of $H_{stokes} = 4.5(2\nu/\omega)^{1/2}$ so a related third non-dimensional group of potential interest would be h/H_{stokes}.

The calculation begins with no flow in the domain. The piston is moved through several cycles (generally 10 for lower Re_e and 20 for higher Re_e) before the flow is nearly periodic. Data are then taken over the last cycle. The grid size used is 128×512 in y and z, respectively, and $h/y_{l/2} = 0.0762$ so a single riblet is resolved with 27 surface points. Figure 16 illustrates the vorticity dynamics over half a cycle for a fairly high Reynolds number, low Strouhal number (Re_e =53.9, St =.339, $h/H_{stokes} = 0.671$). This is one of the more complicated situations because the vortices which are shed travel widely and do not decay rapidly. In the initial frame ($t = 0$) there are vortices present from previous cycles in the periodic sequence and frame $t = \pi/\omega$ represents the same flow as $t = 0$ but a half-cycle later. As the flow moves right ($t = 0$ to $t = \pi/4\omega$), a concentrated region of positive vorticity (B) is swept off the windward side of the riblet and accumulates on the leeward side. Once there, the $+\Omega_x$ vortex B begins inducing the production of negative vorticity on the leeward side ($t = \pi/2\omega$ to

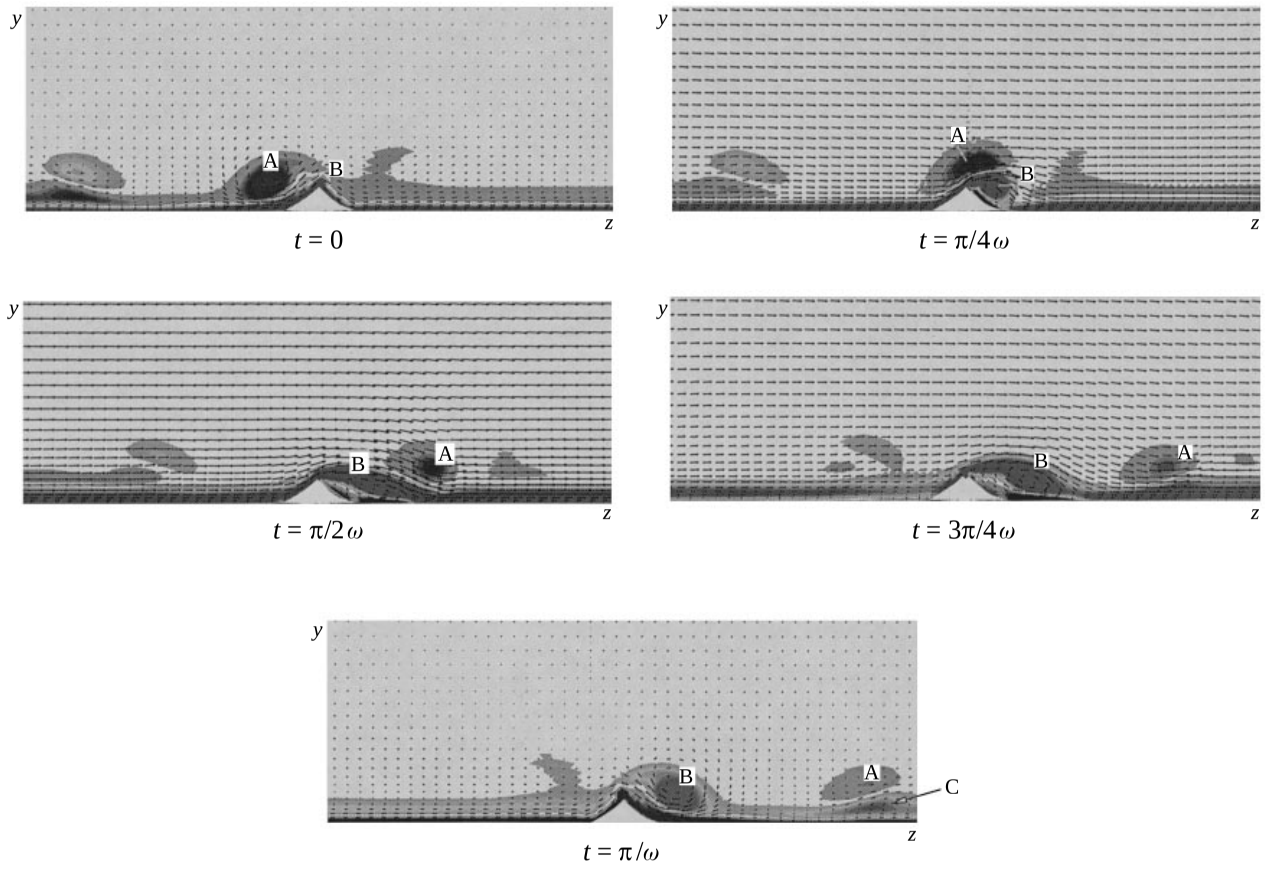

FIGURE 16. Vorticity dynamics during half of a cycle of sinusoidally driven oscillating flow over a riblet. Mean flow to the right first increases and then decreases. A indicates a $-\Omega_x$ vortex formed during the previous half-cycle while B labels the $+\Omega_x$ vortex shed from the riblet tip during this half-cycle. C indicates the vortex patch scooped out of the wall Stokes layer by vortex A.

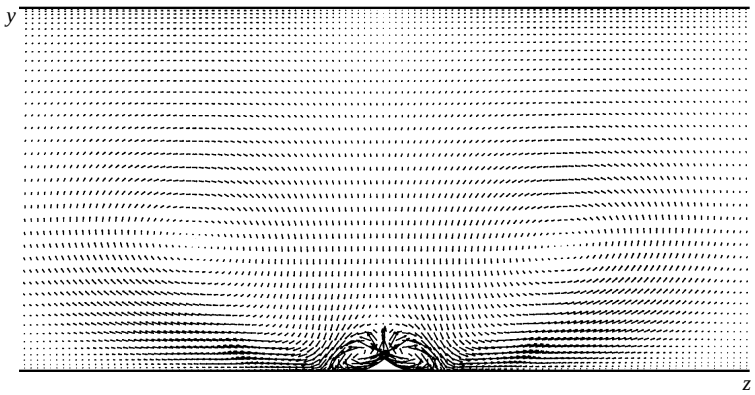

FIGURE 17. Time-average (mean) secondary and tertiary flows for the run presented in figure 16.

$t = 3\pi/4\omega$). As the far-field flow reverses (starting at $t = \pi/\omega$) the B patch of positive vorticity completely separates from the rib. This is as far as the half-cycle shown in the figure illustrates. One can continue to follow the mirror image sequence starting back at $t = 0$ with negative vortex A. The separated vortex A is convected to the right as the Stokes layer vorticity becomes positive. The patch of negative vorticity (A) then scoops up some of the Stokes layer vorticity into patch C ($t = \pi/\omega$) and forms a propagating vortex pair. The scooped circulation (C) is weaker than the scooping vortex A so the new propagating pair will follow a curved counter-clockwise trajectory out and away from the riblet, eventually looping around into a larger merged vortex. The time-average flow over one complete cycle is seen in figure 17.

A careful consideration of the sequence of events explains the origin of the secondary and tertiary vortex pairs seen in figure 17. The secondary flow is caused by the vortex initially shed from the rib tip (vortex A at $t = 0$ and vortex B at $t = \pi/\omega$) and the dramatic upwash the vortex causes as it is blown backwards immediately upon flow reversal. In the turbulent simulations this upwash causes vertical mixing of streamwise momentum and presumably explains why the upwash region over an element is closely associated with large values of $\langle -uv \rangle$. The tertiary flow is now seen to be a result of the accumulation of these shed vortices (and their Stokes layer counterparts like vortex C) on the opposite side of the rib. Preliminary experimental flow visualization studies confirm this sequence of events. These mean flow results clearly resemble those found in the turbulent simulations.

In a turbulent flow the situation would not be as clean. We can better evaluate the effects by exploring a range of the Reynolds and Strouhal number parameter space. Generally, as Re_e is increased, the individual vortices do not diffuse as rapidly and the mean secondary/tertiary flow becomes stronger. When the frequency of oscillation (St) is increased, the fluid does not slosh as widely to the sides during a cycle, the vortical activity is constrained closely about the riblet tip, and the tertiary flow becomes negligible. Figure 18(a) illustrates the mean location of the secondary and tertiary vortex cores for a range of Re_e and St values. As Re_e increases the secondary cores move down while the tertiary cores generally move up. As St values increase the secondary and tertiary core locations move down and closer to the riblet. In figure 18(b) are shown results for the turbulent runs taken from table 1 and experimental and numerical results from various sources. We see that tertiary flow is only found in simulations of turbulent flow over isolated el-

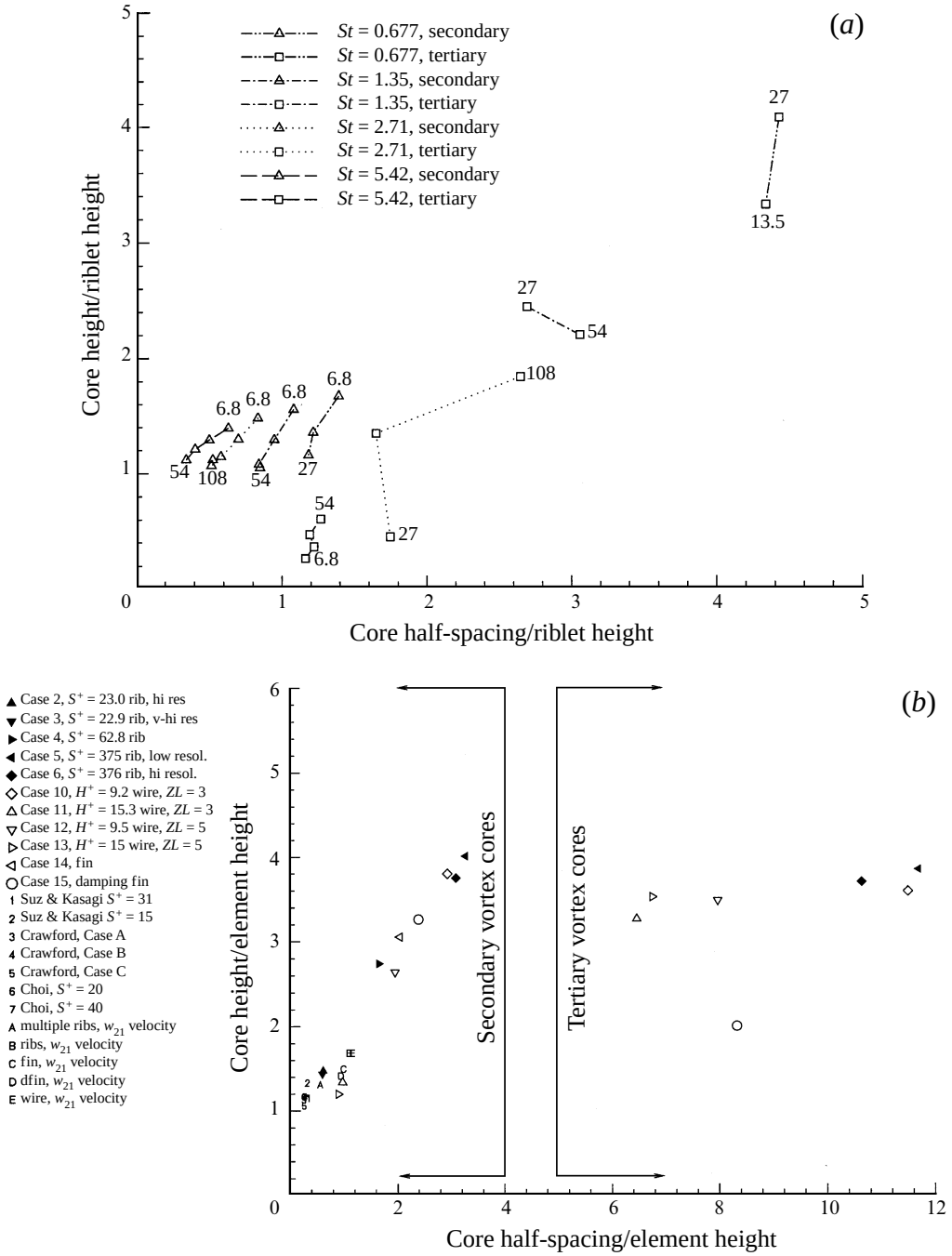

FIGURE 18. (*a*) Mean positions of secondary and tertiary vortex cores normalized by the riblet height near a single riblet subject to sinusoidal cross-flow. Different lines correspond to different Strouhal numbers for either secondary or tertiary vortices. The numbers at the ends of the lines indicate the minimum and maximum Reynolds numbers. Consecutive symbols on a given line correspond to a change in Re_e by a factor of two. (*b*) Mean positions of secondary and tertiary vortex cores for select turbulent DNS, experiments and w_{21} sloshing runs normalized by the element height.

ements. For closely spaced riblets the secondary cores lie quite close to the riblet tips. In fact, considering the different riblet sizes and shapes, the agreement between the various results for turbulent flow over closely spaced riblets is remarkably good. For all the isolated elements except the $H^+ = 15$ wire, the secondary cores are located above and to the side of the element. It may be that the $H^+ = 15$ wire is sufficiently far from the wall that cross-flow can easily pass below the wire and lower the mean secondary core location. In comparing the data for isolated riblets in figures 18(*a*) and 18(*b*), one finds that in fully turbulent DNS the locations of the mean secondary and tertiary cores reflect a much lower Strouhal number than that expected based on a cross-flow velocity energy spectrum over a flat plate.

Figure 19(*a,b*) illustrates how the strength of the secondary flow varies with Re_e and St. In the figure $\overline{V}_{max}$ is the maximum upflow velocity over the rib crest while $\overline{V}_{min}$ is the minimum downflow velocity to the side of the riblet in the downwash created between the secondary and tertiary flows. Stronger mean flows are clearly associated with larger Re_e and smaller St values.

5.2. *Pseudo-turbulent spanwise motion*

What Re_e and St correspond to an actual boundary layer? In a boundary layer there would be a range of frequencies present, each characterized by a different amplitude. Moreover, the perturbation element might itself alter the spectrum of spanwise fluctuations. Suppose, however, to approximate the effect of the near-wall spanwise motion in a turbulent boundary layer, we extract from a numerical simulation the actual spanwise velocity at some point above the wall in a flat-plate boundary layer. We then use that velocity trace as the specified velocity of the piston in the two-dimensional simulations. The height above the wall where the data are taken will determine the amplitude and frequency of the fluctuations. The height chosen was $21l^*$ corresponding to an w_{rms} of $0.81u^*$. This velocity trace is termed w_{21}. A lower height in the boundary layer (like the height of the riblet tip) experiences lower-amplitude fluctuations with a similar frequency distribution. But based on the studies presented above, it was felt more practical to use the slightly higher-amplitude fluctuations of $21l^*$. The riblet Reynolds number of this flow is 7.7. Most of the significant spectral energy is roughly in the range $0.19 < \omega < 4.40$ so a rough range of effective Strouhal numbers would be $0.56 < St < 13.2$. Thus, the w_{21} velocity trace will produce Re_e and St values corresponding to the range explored by the previous periodic forcing studies.

The mean vortex core locations which develop due to w_{21} piston motion for each element used in the turbulent simulations of §§ 3 and 4 are seen in figure 18(*b*). Generally, no tertiary flows are found and the secondary cores lie close to the element tip(s). The strengths of these w_{21} induced flows are summarized in table 2. A summary of the observations for each element follows.

5.2.1. *Single riblet*

For the individual riblet, although a secondary flow develops due to w_{21} cross-flow, it is more confined than in the turbulent runs but of roughly the same peak upflow velocity over the rib crest: $\overline{V}_{max}/w'_{21} = 0.27$ compared to $\overline{V}_{max}/(0.81u^*) = 0.40$ for case 5. One might have expected modest agreement at best because the w_{21} velocity profile is not the same as the actual cross-flow experienced by the riblet in case 5. No substantial tertiary flows are seen with the w_{21} piston motion.

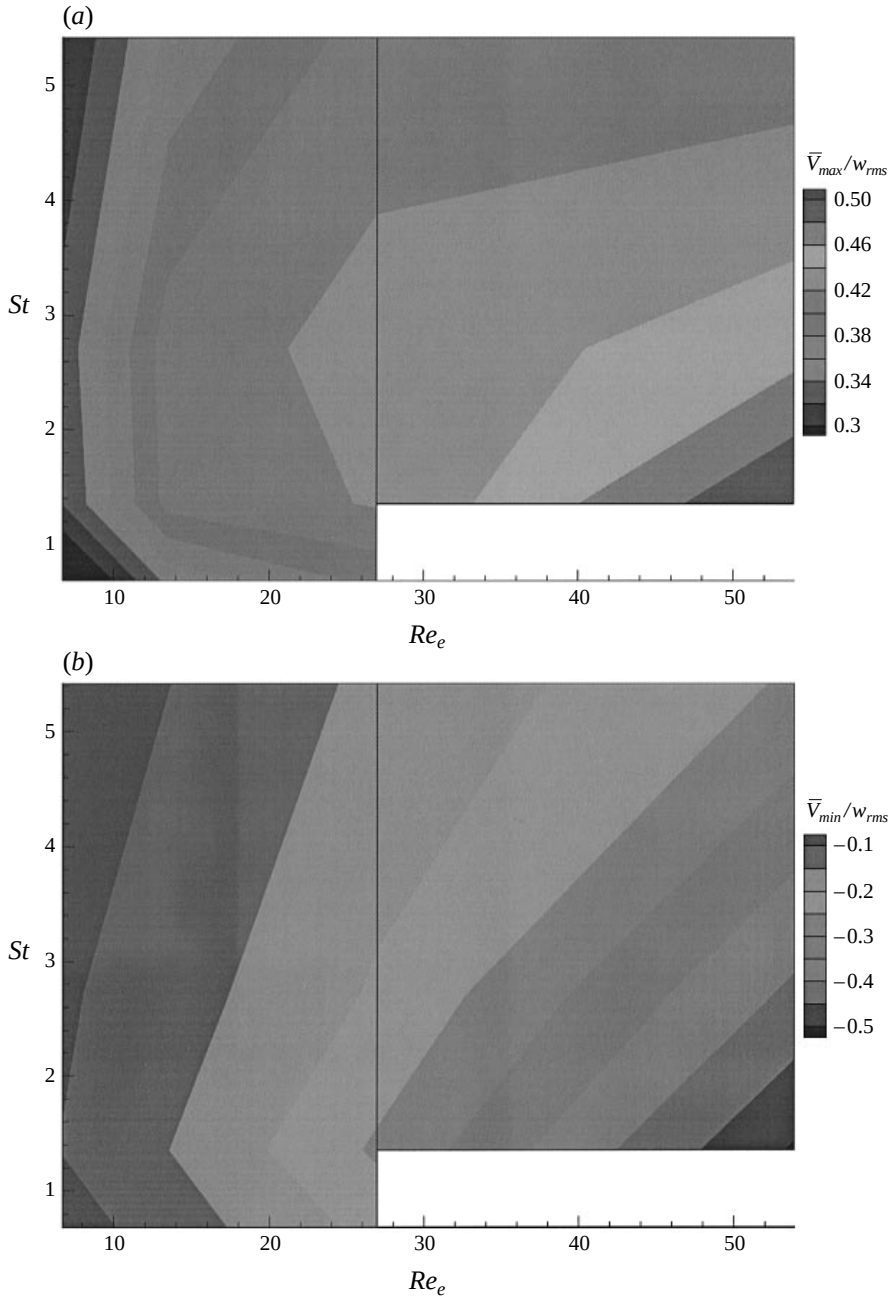

FIGURE 19. Strength of the induced secondary flow near a single riblet subject to sinusoidal cross-flow for various Re_e and St. (*a*) Maximum mean vertical velocity found over the tip of the riblet. (*b*) Minimum mean vertical velocity found in the downwash regions to the sides of the riblet.

5.2.2. *Riblet array*

If we apply the w_{21} velocity trace to a periodic array of closely spaced cusped riblets of the geometry used in §3.1, animations show that only tiny and weak regions of vorticity form near the rib tip and then diffuse quickly; the mean flow has only

Run	$\overline{V}_{max}/w'_{21}$	$\overline{V}_{min}/w'_{21}$
Single riblet	0.271	−0.061
Close riblets	0.220	−0.134
Solid fin	0.303	−0.071
Damping fin	1.083	−0.20
Single slot	0.366	−0.394
Wire at $h/y_{1/2} = 0.0761$	0.222	−0.0362
Wire at $h/y_{1/2} = 0.1181$	0.291	−0.0209

TABLE 2. Strength of mean vertical flows near elements subject to w_{21} cross-flow.

small secondary vortices in agreement with what was found near the case 2 and 3 riblets. Vortices with a tertiary flow orientation exist deep in the riblet valleys but are hardly discernible.

5.2.3. *Single fin*

The w_{21} sloshing flow over a single fin produced essentially the same secondary flow results as found in §5.2.1. The strength of the secondary flow upwash is also similar to that found in the fully turbulent run: $\overline{V}_{max}/w'_{21} = 0.30$ compared to $\overline{V}_{max}/(0.81u^*) = 0.43$ for case 14. If a damping fin is used like that in case 15, the same mean secondary flow pattern is found but the strength of the vortices is increased appreciably to $\overline{V}_{max}/w'_{21} = 1.08$. The increased secondary flow strength right over the fin probably occurs because the damping fin does not apply a vertical viscous drag to slow the vertical flow. Both types of fin lack a clear tertiary flow probably due to the relatively high frequency of the w_{21} oscillations: the vorticity shed by the fin tip hardly has time to move off to the side before it is swept back. Hence, the secondary vorticity only can cause very weak tertiary vortices right near the fin base.

5.2.4. *Slot*

During *sinusoidal* sloshing flow over a slot at modest values of Re_e and St, flow separation can occur and a single vortex fills the slot. When the flow reverses the vortex weakens and rises a bit out of the cavity before diffusing completely. The mean flow consists of a pair of counter-rotating vortices in the slot with downflow along the slot centreline and no tertiary vortices. With a high Re_e (= 108) and small St (= 0.338), as it is washed out of the valley the shed slot vortex can remain intact long enough to scoop up Stokes layer vorticity and form tertiary vortices. The w_{21} velocity field also produces a moderately strong vortex pair in the slot having the cores in line with the slot edges. The presence of such strong secondary flow in a slot is somewhat misleading, however, because in the fully turbulent DNS the single slot is submerged at least 21 wall units below the relatively strong w_{21} oscillations occurring in the buffer layer.

5.2.5. *Wire*

Finally, if a single wire is used with the w_{21} velocity trace only very small and moderately weak secondary flows are found immediately adjacent to the wire. Additional vortices with the tertiary orientation are seen below the secondary vortices, hugging the wire. The perturbations induced by the wire do not appear to interact much with the flat surface and, hence, the tertiary and secondary vortices are nearly symmetric and of the same strength. The huge tertiary vortices found in the turbulent runs are absent in the w_{21} sloshing case.

6. Summary and discussion

The virtual surface approach was used to simulate fully turbulent flow over riblets spaced by various amounts. Grid resolution studies in fully turbulent simulations confirmed that the physical features of the flow were grid resolved. The mean velocity, fluctuating velocity and Reynolds stress contours for the different cases were compared. Based on these results, a simple model for the increase in drag for widely spaced riblets can be described: as the spacing between riblets is increased, the riblets damp the cross-flow fluctuations less and the cross-flow in the valleys becomes stronger (e.g. compare figures 5*d*, 6*d*, and 7*d*). Riblets then no longer provide a cross-flow shield for their neighbours. Strong cross-flow interacts with the more isolated riblets to produce a secondary flow which is associated with vertical mixing (figures 5*e*, 6*e*, and 7*e*) and increased drag.

To test this idea and determine the origin of the secondary flow, turbulent flow simulations were performed over single slots, wires and fins. While single slots produced only weak secondary flows because they were submerged so far below the turbulence, wires produced strong secondary and tertiary flows. Together these simulations show that the riblet crests, rather than the valleys, are most responsible for the secondary flow. The w-damping fin results showed that the secondary flows were not easily explained by tilting of Ω_y or Ω_z vorticity by the mean shear or by Prandtl's secondary flow of the second kind.

It was proposed that the secondary flows are physically explained as a two-dimensional feature involving spanwise sloshing of the flow over the element(s) examined. The sources of the secondary and tertiary flows were explained in terms of the two-dimensional vorticity dynamics. This mechanism was then examined for single riblets for a range of Reynolds and Strouhal numbers in a two-dimensional periodically oscillating flow. If the two-dimensional oscillating flow was made to resemble that in a turbulent boundary layer at $y^+ = 21$, the mean flows over the riblets and other elements reflected the high frequency of such a driving flow.

In some of the cases discussed, the secondary flow is probably best characterized as a form of Prandtl's secondary flow of the *third* kind (Prandtl 1952, p. 149) discussed in greater detail by Schlichting (1979, p. 428). Schlichting points out that a flow caused by small periodic oscillations of a body ($St \gg 1$) "induces a steady, secondary ('streaming') motion at a large distance from the wall as a result of viscous forces" although the magnitude of the streaming motion is independent of the viscosity. The resulting secondary motion is quite similar to that discussed above in the (y, z)-plane. The present simulations show a clear dependence on viscosity. Hence, the analogy with Schlichting's derivation is only partial.

There are two important differences between the piston-forced two-dimensional oscillations and those which occur in a turbulent boundary layer. Whereas the piston maintains a prescribed amplitude and frequency for the velocity field, surface textures below a turbulent boundary layer can locally alter the spanwise velocity. This leads one to believe that the elements tested in the turbulent boundary layer probably altered the spanwise sloshing velocities which in turn created the particular secondary flows. In addition, the turbulent boundary layer has an effective eddy viscosity that is greater than the molecular viscosity of the two-dimensional model.

Improving the drag-reducing utility of riblets or similar elements by increasing their spacing is prevented by the vertical stirring of streamwise momentum induced by spanwise motion and the coincident formation of secondary flows. The results presented here indicate that to design better surface textures one may want to disrupt the formation of secondary flows. It may also be useful to use simple two-dimensional sloshing flow simulations in the design process.

Alternatively, one may view the use of such elements as a method of redirecting turbulent boundary layer spanwise fluctuations into a mean wall-normal line jet along the crest of the element. The idea of having an element that can rectify turbulent motion into directed mean motion is interesting. Perhaps such a device would find application in a heat transfer process or as a low-profile boundary layer turbulator.

The computations were performed at the Texas Advanced Computing Center at The University of Texas at Austin. The work was supported by the Chung Cheng Institute of Technology, Taiwan, ROC, by a grant from Cray Research Inc., and by a computer time grant from the National Partnership for Advanced Computing Infrastructure. Helpful conversations with R. Handler are gratefully acknowledged.

REFERENCES

Bacher, E. V. & Smith, C. R. 1985 A combined visualization-anemometry study of the turbulent drag reducing mechanisms of triangular micro-groove surface modifications. *AIAA Paper* 85-0548.

Bechert, D. W. & Bartenwerfer, M. 1989 The viscous flow on surfaces with longitudinal ribs. *J. Fluid Mech.* **206**, 105–129.

Bechert, D. W., Bartenwerfer, M., Hoppe, G. & Reif, W. E. 1986 Drag reduction mechanism derived from shark skin. In *15th Congress of the Intl Council of Aeronautical Sciences, Sept. 7-12, London, UK*. ICAS-86-1.8.3.

Bechert, D. W., Bruse, M., Hage, W. & Meyer, R. 1997*a* Biological surfaces and their technological application - laboratory and flight experiments on drag reduction and separation control. *AIAA Paper* 97-1960.

Bechert, D. W., Bruse, M., Hage, W., Van der Hoeven, J. G. T. & Hoppe, G. 1997*b* Experiments on drag-reducing surfaces and their optimization with an adjustable geometry. *J. Fluid Mech.* **338**, 59–87.

Bernard, P. S., Thomas, J. T. & Handler, R. A. 1993 Vortex dynamics and the production of Reynolds stress. *J. Fluid Mech.* **253**, 385–419.

Brooke, J. W. & Hanratty, T. J. 1993 Origin of turbulence-producing eddies in a channel flow. *Phys. Fluids* A **5**, 1011–1022.

Choi, H., Moin, P. & Kim, J. 1991*a* On the effect of riblets in fully developed laminar channel flows. *Phys. Fluids* A **3**, 1892–1896.

Choi, H., Moin, P. & Kim, J. 1993 Direct numerical simulation of turbulent flow over riblets. *J. Fluid Mech.* **255**, 503–539.

Chu, D., Henderson, R. & Karniadakis, G. 1992 Parallel spectral-element-Fourier simulation of turbulent flow over riblet-mounted surfaces. *Theor. Comput. Fluid Dyn.* **3**, 219–229.

Chu, D. & Karniadakis, G. 1993 The direct numerical simulation of laminar and turbulent flow over riblets. *J. Fluid Mech.* **250**, 1–42.

Coustols, E. & Savill, A. M. 1992 Turbulent skin-friction drag reduction by active and passive means: parts 1 and 2. *Special Course on Skin-Friction Drag Reduction*, March 2-6, pp. 8–1 to 8–55, *AGARD Rep.* 768.

Crawford, C. H. 1994 The structure and statistics of turbulent flow over riblets. Masters thesis, Princeton University.

Crawford, C. H. & Karniadakis, G. E. 1996 Reynolds stress analysis of controlled wall-bounded turbulence. *AIAA Paper* 96-2008.

Demuren, A. O. & Rodi, W. 1984 Calculation of turbulence-driven secondary motion in non-circular ducts. *J. Fluid Mech.* **140**, 189–222.

Djenidi, L., Squire, L. C. & Savill, A. M. 1991 High resolution conformal mesh computations for V, U or L groove riblets in laminar and turbulent boundary layers. In *Recent Developments in Turbulence Management* (ed. K. S. Choi), p. 239. Kluwer.

Gessner, F. G. 1973 The origin of secondary flow in turbulent flow along a corner. *J. Fluid Mech.* **58**, 1–25.

GOLDSTEIN, D., ADACHI, T. & IZUMI, H. 1993*a* Modeling flow between concentric vibrating cylinders with an external force field. In *Proc. AIAA CFD Meeting, Orlando, FL.*

GOLDSTEIN, D., HANDLER, R. & SIROVICH, L. 1993*b* Modeling a no-slip flow boundary with an external force field. *J. Comput. Phys.* **105**, 354–366.

GOLDSTEIN, D., HANDLER, R. & SIROVICH, L. 1995 Direct numerical simulation of turbulent flow over a modelled riblet covered surface. *J. Fluid Mech.* **302**, 333–376.

HANDLER, R. A., HENDRICKS, E. W. & LEIGHTON, R. I. 1989 Low Reynolds number calculation of turbulent channel flow: a general discussion. *NRL Mem. Rep.* 6410, pp. 1–103.

HUSER, A. & BIRINGEN, S. 1993 Direct numerical simulation of turbulent flow in a square duct. *J. Fluid Mech.* **257**, 65–95.

JIMENEZ, J. & MOIN, P. 1991 The minimal flow unit in near-wall turbulence. *J. Fluid Mech.* **225**, 213–240.

KIM, J., MOIN, P. & MOSER, R. 1987 Turbulence statistics in fully developed channel flow at low Reynolds number. *J. Fluid Mech.* **177**, 133–166.

KRAMER, M. 1937 Einrichtung zur Verminderurg des Reibungswide stands (Device for Reducing the Frictional Resistance). German Patent no. 669897, March 17.

LUCHINI, P., MANZO, F. & POZZI, A. 1991 Resistance of a grooved surface to parallel and cross-flow. *J. Fluid Mech.* **228**, 87–109.

PARK, S.-R. & WALLACE, J. M. 1993 Flow field alteration and viscous drag reduction by riblets in a turbulent boundary layer. *AIAA Paper* 93-3256.

ROBINSON, S. K. 1991 Coherent motions in the turbulent boundary layer. *Ann. Rev. Fluid Mech.* **23**, 601–639.

PRANDTL, L. 1952 *Essentials of Fluid Dynamics.* Blackie and Son Ltd., London and Glasgow.

SCHLICHTING, H. 1979 *Boundary-Layer Theory*, 7th edn. McGraw-Hill.

SUZUKI Y. & KASAGI, N. 1994 Turbulent drag reduction mechanism above a riblet surface. *AIAA J.* **32**, 1781–1790.

WALSH, M. J. 1990 Riblets. In *Viscous Drag Reduction in Boundary Layers* (ed. D. Bushnell & J. Hefner). Progress in Astronautics and Aeronautics, vol. 123, pp. 203–259. AIAA.